Ceramics International 52 (2026) 17714–17731

Contents lists available at ScienceDirect

Ceramics International

journal homepage: www.elsevier.com/locate/ceramint

Chemical resistance of vitreous enameled cast iron

Büşra Karakaş [a,b], Nicolò Mattei [a], Luca Benedetti [a], Stefano Rossi [a,*]

[a] Department of Industrial Engineering, University of Trento, Via Sommarive 9, 38123 Trento (TN), Italy
[b] Department of Materials Engineering, University of Miskolc, Egyetem út 1, 3515 Miskolc, Hungary

ARTICLE INFO

Handling Editor: Dr P. Vincenzini

Keywords:
Cast iron
Porcelain enamel coating
Chemical resistance
Chemical element extraction
Water safety

ABSTRACT

This study investigates the chemical resistance of vitreous enamel coatings applied to cast iron substrates under water environments. Two SiO_2-Na_2O-B_2O_3-CaO-Al_2O_3-based frits (ground G1 and G2) were developed to investigate the influence of chemical composition, heat-treatment temperature, and titanium glaze top-layer application on elemental release behaviour. The coatings were heat-treated at different temperatures (740 °C and 780 °C). They were subjected to distilled water leaching tests to assess their durability through inductively coupled plasma (ICP). The results show that the G2 coating exhibited significantly lower elemental release compared to G1 due to the incorporation of Li_2O and TiO_2. Furthermore, the heat-treatment temperature had no prominent influence on the performance of G2. For G1 and G2, the application of a glaze top layer effectively reduced the release of hazardous elements such as Co, Mn, and Cr. However, incomplete surface coverage of the glaze top-layer left localized areas susceptible to leaching and resulted in localized attack. In summary, compositional optimization and glaze top-layer proved to be the most effective approach for enhancing the chemical resistance of vitreous enamel coatings on cast iron.

1. Introduction

The cost of corrosion in the United States is approximately USD 276 billion per year, which equals approximately 3% of the nation's gross domestic product (GDP) (1998) [1], thereby corrosion is one of the issues that needs to be addressed. Furthermore, the CO_2 emissions associated with steel production to replace corroded steel are estimated to account for approximately 4.1% to 9.1% of total emissions by 2030, comprising the US and EU regions [2]. Implementing best practices in corrosion management methods has the potential to reduce these emissions significantly. Among these methods, the utilization of protective coatings is the most effective and economical method [3] such as organic coatings [4], metallic coatings [5], composite coatings [6], and inorganic coating, including ceramic [7] and enamel coatings. Generally, the application of protective coatings to metallic structures protects against atmospheric corrosion and aqueous environments [7]. This approach aims to restrain the progression of corrosion processes, thereby preserving the structural functionality and extending the service life of products. The effective implementation of corrosion control technologies could reduce corrosion-related losses by 15–35% [8].

Porcelain enamel is a vitreous, glass-like coating that is employed on metal substrates and formed by heat treatment at high temperatures between 500 and 900 °C [9]. This heat treatment generates a permanent bond between the enamel and the metal substrate through chemical and physical interactions.

Enamel coatings are utilized in technical and precise engineering in various industrial applications. These applications comprise a wide range of areas, such as aerospace [10], kitchen utensils [11], automative [12], architecture [13], pipelines [14], nuclear industry [15], with various types of metallic substrates, including steel [16], cast iron [17], aluminium [18], nickel-based alloys [19], titanium alloys [20], and so on. Vitreous enamel coatings have come up as significantly efficient protective coatings for metallic substrates that are subjected to harsh environments, thanks to their mechanical hardness, superior chemical and thermal stability, and corrosion resistance [21]. Porcelain enamel layers protect the metal substrate from corrosion by acting as a barrier, separating it from the aggressive environment. Their durability against aggressive media is the key criterion for enamel coatings, as their corrosion resistance under exposure to alkaline, acidic, saline, and high-temperature conditions [22,23,24].

In the alkaline corrosion, microstructural degradation stages responsible for enamel failure arise in a generalized manner, resulting in dissolution of the glassy matrix [25].

The resilience of enamel coatings can be tailored through their

* Corresponding author.
E-mail address: stefano.rossi@unitn.it (S. Rossi).

https://doi.org/10.1016/j.ceramint.2026.02.353
Received 7 January 2026; Received in revised form 29 January 2026; Accepted 22 February 2026
Available online 23 February 2026
0272-8842/© 2026 The Authors. Published by Elsevier Ltd. This is an open access article under the CC BY license (http://creativecommons.org/licenses/by/4.0/).

chemical composition. For example, increasing the SiO_2 content while reducing the borax concentration improves resistance to hot water and alkaline media, resulting in enhanced structural rigidity [26,27].

Refractory oxides such as TiO_2, ZrO_2, Al_2O_3, Cr_2O_3, and MgO are incorporated to adjust viscosity, enhance mechanical strength, and chemical durability [28,29,30,31]. They delay the leaching of alkali and alkaline earth ions and slow network degradation, improving enamel durability under oxidative and high-temperature environments [32,33]. In addition, ZrO_2 or ZrB_2-reinforced considerably increases alkali resistance with the generation of zirconosilicates and zirconates that block mobile alkali ions such as Na^+ and reinforce the glass network [28, 32,34,35]. These additives reduce corrosion current density and mass loss, improving structural integrity even after long-term exposure in saline and alkaline solutions [36].

The corrosion mechanism under acidic conditions typically involves the hydrolysis of glass-forming polyhedra such as [SiO_4], [BO_3], [BO_4], and [AlO_6] due to the leaching of mobile alkali ions, which weakens the enamel network [32]. Furthermore, compared to slurry-based enamels, powder enamel coatings offer better protection due to their denser microstructure [37]. It leads to enhanced corrosion resistance due to limiting ion diffusion pathways [38]. Recent studies have also underlined the performance of low-temperature enamels (e.g., aluminophosphate-based systems) that possess durable behavior across a pH range of 3 to 10 [39]. Enamel have been investigated for porous aluminum foams, obtaining prolonged protection during accelerated corrosion testing [40].

In addition to other corrosion media, water corrosion also significantly influences the durability of the enamel coatings, particularly in applications such as water pipelines. Enamel coatings provide pipelines operating at higher temperatures up to 400 °C with a safety factor of approximately 1.25 due to their high glass transition temperatures [41]. Nevertheless, corrosion formation within pipelines affects hydraulic efficiency and increases energy demand, which may subsequently lead to leakage as a result of pitting corrosion [42,43]. Water corrosion of enamel coatings typically initiates with an ion-exchange behavior, where alkali ions are leached out and hydronium ions (H_3O^+) and water molecules enter the glass, forming a hydrated, alkali-deficient gel layer [44].

Despite its importance, the interaction between water and vitreous enamels remains insufficiently studied to the best of our knowledge. While previous research has examined water corrosion in vitreous enamels in various applications [23,27,33], cast iron substrates with different enamel coating cycles present unique challenges and opportunities. Cast iron is a material widely used in the field of water transportation, such as in pipelines, pumps, and other hydraulic components [45]. Although, in many environments, this material shows greater resistance to corrosion compared to steel, it is often necessary to improve its corrosion behavior in order to prevent contamination of the transported fluid. As with steel, enameled porcelain coating can also be an excellent solution for cast iron [17].

Substantially, the corrosion resistance of enamel is adjusted by the relation between glass composition, microstructure, and processing parameters [23,27,33]. Optimal tailoring of the formulation and application techniques can significantly enhance longevity under various harsh environments, including hot water, acidic and alkaline solutions, salt spray, and high temperatures. This study aims to comprehensively investigate the ion leaching mechanism from enameled cast iron under distilled water conditions. Parameters such as temperature and enamel chemical composition were analyzed. The goal is to provide a broad understanding of how these factors influence the chemical resistance of enameled cast iron. A very important aspect when applying porcelain enamels to drinking water is assessing the release of certain hazardous elements, such as Cr, Co, and Mn. Ground coatings with adhesion-promoting oxides ensure strong bonding to cast iron. These elements, however, are necessary to achieve a layer with good adhesion. A second, transparent layer (glaze) was applied as the final coating to assess its ability to limit the release of these hazardous elements. Titanium-based enamels are favored for their cost-effectiveness, opacity, and performance, and provide durability, chemical resistance, and aesthetics [46].

2. Materials and Methods

2.1. Materials

The samples utilized in this study were produced in the industrial laboratory of Emaylum Italia (Chignolo d'Isola, BG, Italy). The enameled cast iron substrates utilized are standard, measuring 100 mm x 100 mm size. Two different frits are used to obtain the first ground layers (G1 and G2). A transparent top coat (glaze) was then deposited, starting from a titanium white-top coating frit (T1/T2). The chemical composition of used frits for producing the ground and top layer is given in Table 1.

The rationale for selecting the chemical compositions of the different layers was as follows. G1 exhibits the typical composition of enamel used for cast iron substrates. Two main approaches can be adopted to improve the chemical resistance of the enamel: the addition of oxides that enhance chemical durability by reducing alkali mobility (TiO_2), or the improvement of enamel fusibility (Li_2O), leading to a denser glassy structure [46].

A second strategy consists in applying a transparent protective top layer acting as a barrier, with a composition free of hazardous species.

Initially, each ground layer was applied to the cast iron substrates, and subsequently, a white top layer was employed on the dried ground layer. All layers were spray-coated.

In this study, a specific heat-treatment profile was employed, consisting of 2 coating applications and 1 firing treatment cycle (2A/1F). Employing ground and top coating rather than a single layer, along with 2 coatings and 1 firing, is commonly used. Although technically challenging and limiting the broader adoption of single-layer coatings, this approach allows for the production of high-quality enamel.

The sample codes, heat-treatment profile, and thickness are given in Table 2. Two firing temperatures were considered at 740 °C and 780 °C for 12 min to evaluate the temperature effect on the chemical resistance of enamels. The G1/40 sample was produced using G1 frit and heat-treated at 740 °C. The T1/40 sample is composed of the G1 frit as the ground coating and a top layer applied above it, also heat-treated at 740 °C. Similarly, G2/40 was produced using only G2 frit and heat-treated at 740 °C, whereas T2/40 consists of G2 as the ground coating along with a top coating. In contrast, G2/80 was produced using only G2 frit, and T2/80 was prepared with the G2 frit and top coating; however, it was subjected to a higher heat treatment at 780 °C.

For economic reasons and to minimize residual stresses in the coated cast iron component, the lowest possible firing temperatures that still allow adequate frit sintering are employed. Accordingly, an initial firing temperature of 740 °C was selected. However, since higher firing temperatures are known to promote sintering, an increased temperature was also investigated in order to assess its effect on the chemical resistance of the enamel.

2.2. Characterization

Morphology, microstructure, and cross-section of enamel coatings were examined using a scanning electron microscope (SEM, Jeol JSM IT 300, Tokyo, Japan), coupled to an Energy Dispersive X-ray microanalysis system (EDS). After mechanical polishing with a 1 μm diamond paste, the cross-section of the samples was observed by a microscope. EDS analysis was conducted to map the elements before and after exposure to distilled water.

The analysis and quantification of released elements were employed with Inductively Coupled Plasma (ICP) spectroscopy. Following the previously established setup [47], pure distilled water (conductivity: 6 μS) at room temperature was contacted with enameled cast iron samples

Table 1
Chemical composition of frits used in the study (%wt).

Layers	SiO_2	B_2O_3	$Na_2O + K_2O$	$CaO + Al_2O_3$	CoO	MnO_2+Fe_2O_3	CuO	TiO_2	ZnO	LiO_2
G1, Ground	40	25	18	7	1	8	1	/	/	/
G2, Ground	40	18	19	6	1	6	1	8	/	3
Top layer	54	18	17	/	/	/	/	5	6	/

Table 2
Sample abbreviation and experimental design.

Sample Code	Heat-Treatment	Coating Cycle	Thickness (μm)
G1/40	740 °C	Ground 1	288±14
T1/40		Ground 1+Top	344±34 (total) 88 (top, avg)
G2/40		Ground 2	319± 9
T2/40		Ground 2+Top	436 ±10 (total) 150 (top, avg)
G2/80	780 °C	Ground 2	364±20
T2/80		Ground 2+Top	383±80 (total) 111(top, avg)

for a total duration of 10 days. Distilled water was chosen as the electrolyte instead of drinking water because there is no standardized composition for drinking water, and, more importantly, distilled water is more aggressive toward the enamel, promoting greater element extraction due to the larger concentration gradients between the enamel and the water.

The solution was gathered and substituted with fresh distilled water at predetermined intervals (2, 4, 6, 8 and, 10 days) to prevent saturation influences and maintain leaching conditions. The gathered solutions were subsequently analyzed by ICP (PerkinElmer Avio^{TM} 550 Max, PerkinElmer, Waltham, US) to quantify the concentrations of released specific ions, including titanium, potassium, sodium, and silicon.

The 10-day immersion period adopted in this study was not intended to reproduce the full service life of the coating, but to provide an accelerated and controlled assessment of early-stage degradation mechanisms at the coating–environment interface. Short-term immersion tests are commonly used to promote rapid ingress of aggressive species and activate physicochemical processes that would otherwise occur over much longer timescales. In the case of enamel coatings, the most significant changes in surface chemistry and microstructure occur during the initial exposure period, justifying the selection of a 10-day timeframe as a compromise between experimental feasibility and the need for measurable and reproducible degradation data.

The focus was on potentially toxic elements naturally present in the enamel, such as cobalt (Co) and manganese (Mn). Heavy metals such as lead (Pb), cadmium (Cd), and arsenic (As) are indeed key elements regulated by international drinking water standards. These elements were not included in the ICP analysis because they are not present in the composition of the cast iron substrate or in any of the enamel layers applied.

3. Results & Discussion

3.1. Microstructural analysis/investigation of enamel

Figure 1 depicts the microstructural analysis of the cast iron substrate using SEM. The chemical composition of the cast iron was determined using EDS, which revealed the following percentages: C (6.49%), Si (2.40%), Fe (90.05%), P (0.59%), S (0.15%), and Mn (0.32%). The cast iron used in this study is composed of fine and uniform graphite, pearlite, and ferrite structures (Figure 1). Pearlite, ferrite, and graphite phases in cast iron significantly influence the integrity of the enamel and its thermal behavior during enameling. Heat-treatment below the eutectic temperature (740-780 °C) [48] reduces structural

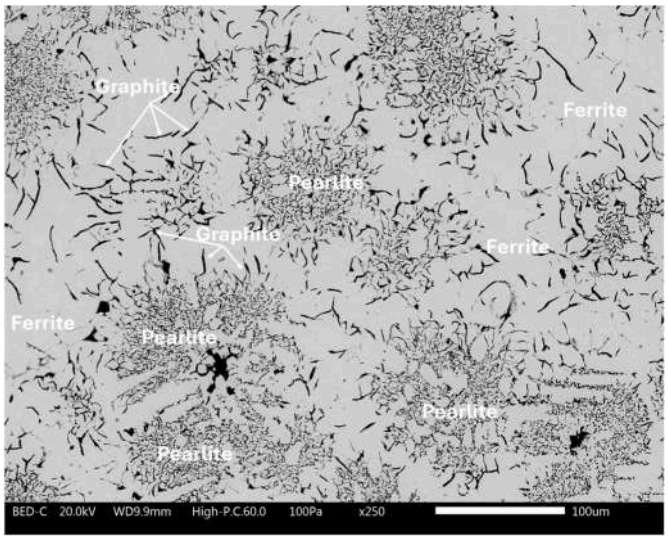

Figure 1. SEM microstructure of cast iron substrate.

changes, internal stresses, and dimensional variations. Moreover, microstructural features such as graphite distribution influence bonding chemistry and quality [49–51]. For gray, thin-walled castings, optimal enamel adherence is achieved with fine, uniform ferrite-graphite and pearlite-graphite structures, as obtained from used cast iron. Furthermore, enameling was considered at 740 °C and 780 °C to minimize dimensional changes and improve adherence.

Cross-section images of G1/40 and T1/40, G2/40 and T2/40, and G2/80 and T2/80 are displayed in Figure 2, Figure 3, and Figure 4, respectively. All samples possess uniform structure in terms of variations of compositional contrast, as shown in Figures 2b-d, Figures 3b-d and, Figures 4b-d. All samples generated in this study accomplished adherence, since the interface through the cast iron and enamel structure is obvious, as can be seen in Figure 2b, Figure 3b and, Figure 4d. Bubble formation is one of the inevitable morphological properties of the enamel; hence, all samples have their own bubble structure. As shown in Figure 2a, G1/40 exhibits larger bubbles, whereas G2/40 (Figure 3a) displays a wider distribution, including both larger and smaller bubbles. This demonstrates that while G2 enamel is prone to generating smaller bubbles along with larger bubbles, larger bubbles are prominent in G1 enamel morphology. This is likely related to the fact that, at equal concentrations of Na_2O and K_2O, Li_2O helps lower the melting temperature.

Adhesion between cast iron and enamel occurs due to oxide formation (FeO, Fe_3O_4, Fe_2O_3), which encourages chemical bonding at the interface [52]. Ion exchange enriches the enamel with metal oxides, enabling metal-to-metal bonding and enamel durability during heat treatment [53]. However, during either heat treatment or slow cooling, the decomposition of cementite (Fe_3C) releases hydrogen and carbon. It may generate gas voids or react with iron and carbon to form hydrogen, water vapor, carbon oxides, and methane, resulting in bubble formation [54].

On the other hand, the difference in bubble formation between G2/80 (Figure 4a) and G2/40 (Figure 3a) appears to be less significant. Regardless of the process parameters, including the frit used,

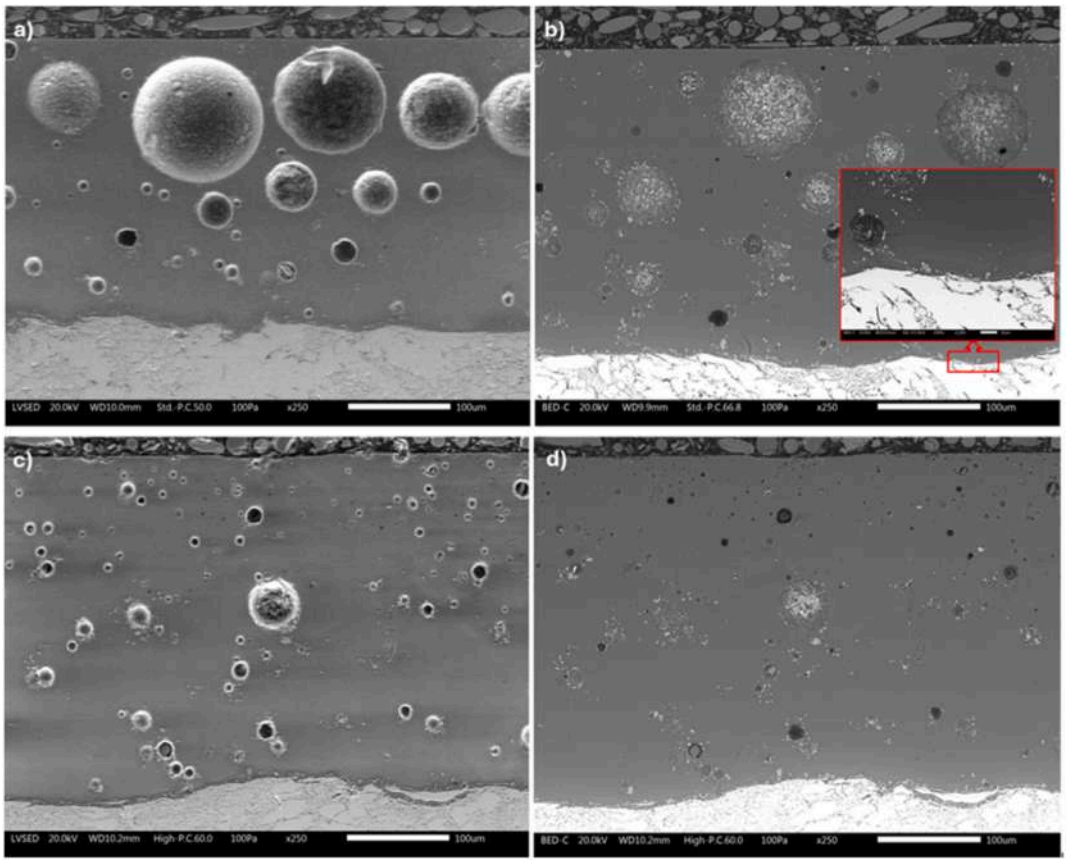

Figure 2. SEM cross-section images of G1/40 (a) and (b), T1/40 (c) and (d). Images a) and c) were taken in SED mode, whereas b) and d) were taken in BED mode.

temperature, and thickness, the number of small bubbles increased, and no large bubbles exist in the structures of top-coated-cast irons (Figures 2c, 3c and, *4c*). In top-layer applications, the enamel fuses more extensively with the substrate and facilitates better gas release, resulting in more compact, defect-resistant microstructures, as reported in the literature [55]. Therefore, increasing the number of coating cycles lowers porosity and enhances resultant coating integrity.

A similar tendency can be observed in the surfaces of the samples, as shown in Figure 5. Top-coated-enamels (Figures 6a, 6c and, *5e*) demonstrate small-sized defects, whereas ground-coat-enamel has larger-sized defects regardless of the process parameters (Figures 5b, 5d and, *5f*). Achieving a defect-free surface on enameled cast iron remains a significant challenge, and variations in cast iron composition aggravate the issue of surface continuity [56,57].

All ground-coated samples possess white crystal-like particles due to precipitation of Fe, Cr, and Al oxides during the firing treatment of the enamels, as can be seen in Figures 5a, 5c and, *5e*. Facilitation of top-layer coating led to the particled-ground coating being covered, resulting in a smooth surface (Figures 5b, 5 d and, *5f*). T2/40 has a smoother surface among the other samples due to the highest thickness value (150 μm). Thicker top-layer enables covering all ground-coating (Figure 5d), while T1/40 (88 μm), T2/80 (111 μm) remain uncovered in some areas, hence precipitated oxides generated due to ground coating compositions were observed (Figures 5b and 5f, lighter circular areas).

The chemical mapping of all samples analyzed in this study is shown in Figures 7 to 11. The elemental mappings correlated with the overall chemical composition listed in Table 1. The most common oxides, and those most likely to be affected by distilled water, are comprised of these mappings. From a compositional perspective, the frits used consist of three groups of oxides: network formers (e.g., SiO_2), network modifiers (e.g., Na_2O, K_2O, CaO), and intermediates (e.g., Al_2O_3, ZnO, MgO) [58]. In addition, adherence oxides (e.g., CuO, CoO, MnO) improve bonding at the coating/cast iron interface [59]. These oxide groups are significant in shaping the microstructure, chemical durability, and overall features of enamel coatings [60].

Figure 6 demonstrates the chemical mapping of G1/40. In correspondence with the precipitated of the Cr and Fe, and in some areas, Al, signals increase.

Figure 7 demonstrates the chemical mapping of T1/40. Due to the presence of the titanium white top coating, this element is also detected in the mapping. The microstructure appears more inhomogeneous compared to G1/40. The coarse compounds observed originate from the ground frit and are subsequently covered by the top coating. In certain regions (circular areas with light point-like parts) where the ground layer is not covered by a glaze coating, a higher signal due the presence of Cr- and Fe-rich coarse particles can be clearly identified along with Al-rich particles. In this area also the calcium signal, present only in the ground layer, is higher.

The thickness of the top layer can be defined so as to avoid the presence of ground areas that are not completely covered, which would otherwise constitute preferential sites for attack and leaching of potentially hazardous elements present in the ground.

Figure 8 shows the chemical mapping of G2/40 produced using the ground 2 frit. Surface porosity is evident. Compounds, mainly rich in Cr and Fe, along with Al-containing oxides, are also observed.

Figure 9 shows the chemical mapping of T2/40. The titanium-based top layer completely covers the ground layer, resulting in a very uniform appearance. Unlike other top-coated samples, Fe- and Cr-rich coarse structures are rarely observed, along with a few Al-rich particles.

Figure 10 presents the chemical mapping of G2/80, prepared using ground 2 frit at a higher firing temperature. Similar to G2/40 (Figure 9), coarse Al-rich oxides are clearly visible, together with Cr- and Fe-rich particles formed along the surface. Some surface defects are also detected, but to a lesser extent, probably because the higher firing

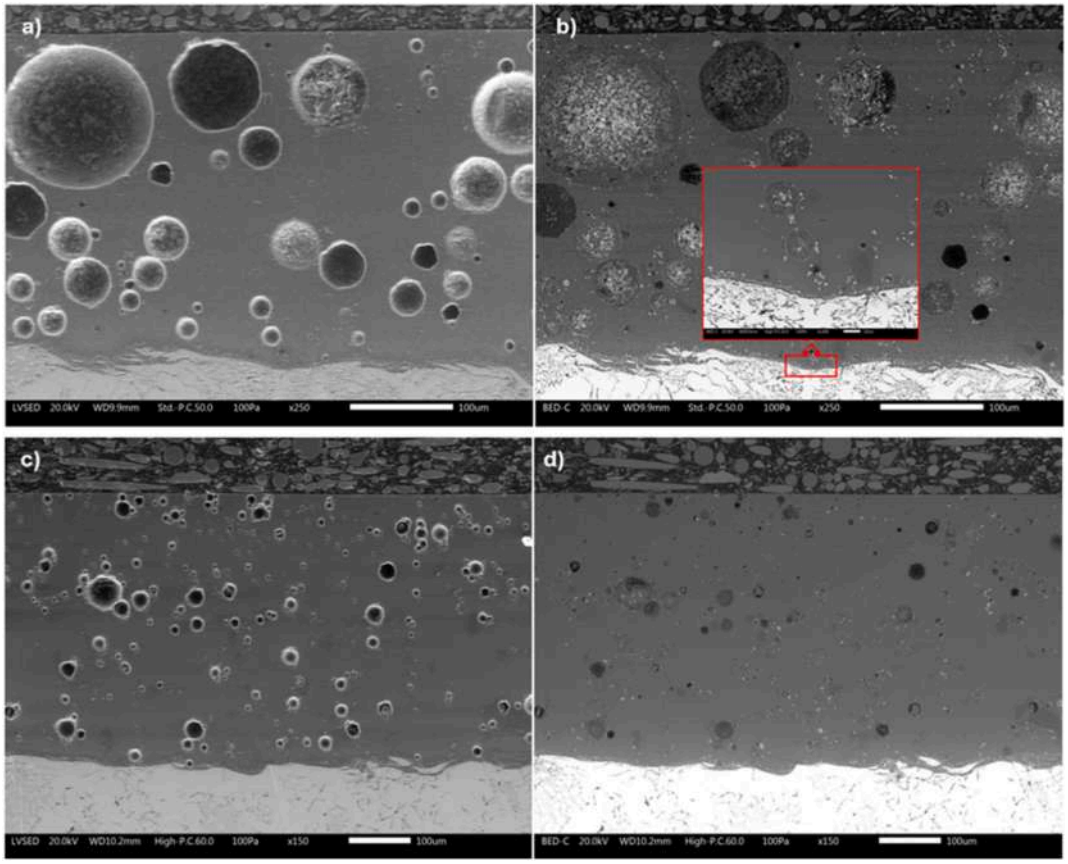

Figure 3. Cross-section images of the G2/40 a) and b), T2/40 c) and d). Images a) and c) were taken in SED mode, whereas b) and d) were taken in BED mode.

temperature allows for easier release of gas bubbles and improved flow of the glass layer.

Figure 11 shows the chemical mapping of T2/80. In this sample, the glaze top coating does not completely cover the ground layer. Therefore, Cr-, Fe-, and Al-rich particles composed from the ground 2 frit are clearly visible in some uncovered areas. Consequently, the surface exhibits a relatively heterogeneous structure. This is probably due to the thinner glaze layer.

3.2. ICP analysis after exposing the distilled water

Figure 12 illustrates the leaching behavior of elements from the enameled samples after exposure to distilled water. The results clearly indicate that Ground 1 exhibits significantly lower chemical resistance compared to Ground 2, since the release of all the elements at the same firing temperature is greater. It is evidenced particularly by measurable losses of alkali elements. In G1/40, alkali elements such as Na and K (Figures 12g and d), show high initial release, which decreases in the mid-phase of testing but rises again towards the end of the exposure period. It indicates an initial rapid leaching, followed by partial stabilization and subsequent reactivation of the leaching process. Silicon (Figure 12h) shows a deterioration trend, with its concentration fluctuating but generally increasing over time. This shows a gradual network breakdown of the glassy phase. Magnesium (Figure 12e) shows a tendency to increase as the exposure continues. This is due to the mobilization of alkaline earth elements from the matrix over longer durations. Considering the differences in composition between the two ground layers, Li_2O helps lower the melting temperature, allowing for a more compact structure. Furthermore, TiO_2 increases chemical resistance by tending to strengthen the glass network, reducing the mobility of alkalis and therefore their extraction.

Consistent with the EDS analyses, the element release in G2/40 and G2/80 is extremely low. No differences are observed due to the higher treatment temperature. In particular, Figures 12d, 12g and, *12h* show that sodium, potassium, and silicon are absent in the leachate, indicating that Na has not been released, K and Si remain stable, and the network structure has not been disrupted, thus preventing visible corrosion. Ground 2 demonstrates excellent stability, exhibiting only minimal losses of Mg (Figure 12e) and Ca (Figure 12a) and no detectable Na or K, thereby confirming its superior chemical durability.

As the observed attack mainly affects the outermost layers of the coating, thickness does not appear to be a determining factor for element release from ground layers.

Thickness becomes more relevant when considering the top layer. In fact, a greater thickness reduces the likelihood of exposed ground areas and, consequently, the release of potentially hazardous elements.

The application of the top layer (Sample T1/40) provides partial protection. Effectively reduces the release of hazardous metal oxides such as Cr (Figure 12c), but does not inhibit the leaching of Co and Mn (Figure 12b and 12f).

This incomplete protection may be attributed to microstructural features observed in the surface micrographs and EDS analyses. It reveals that the top layer does not fully cover the ground coating, leaving localized “islands” enriched in Fe, Mn, and Cr that act as weak points for leaching. While Cr release is strongly suppressed, Na and K still demonstrate extensive leaching throughout the exposure. The highest release occurs during the initial stages and then gradually decreases, although it does not disappear completely. When the top layer is applied to Ground 2 (T2/40), a prominent increase in alkali element release is observed during the first days of exposure.

Figures 12d, 12g and, 12h show that Na, K, and Si decrease over time but remain significantly higher than in the uncoated G2/40 sample. It shows that the top layer introduces alkali leaching despite blocking hazardous elements, including Co, Mn, and Cr (Figure 12b, 12f and,

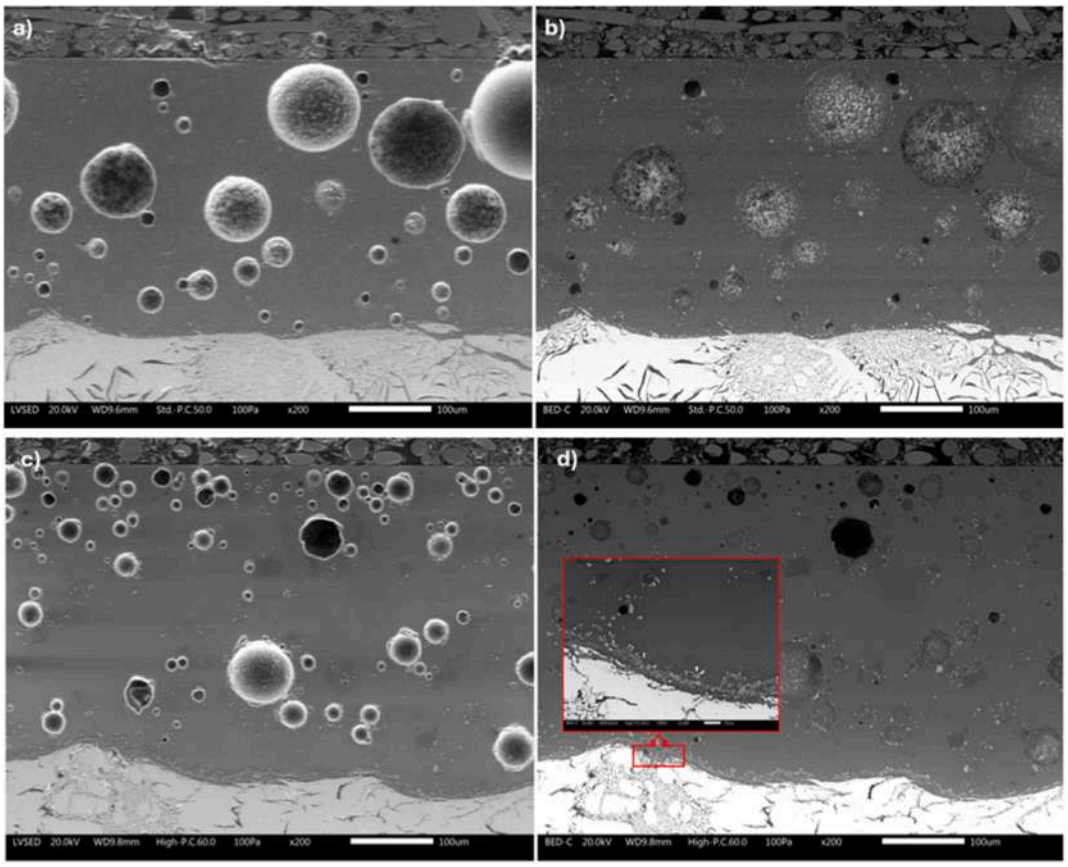

Figure 4. Cross-section images of the G2/80 a) and b), T2/80 c) and d). Images a) and c) were taken in SED mode, whereas b) and d) were taken in BED mode.

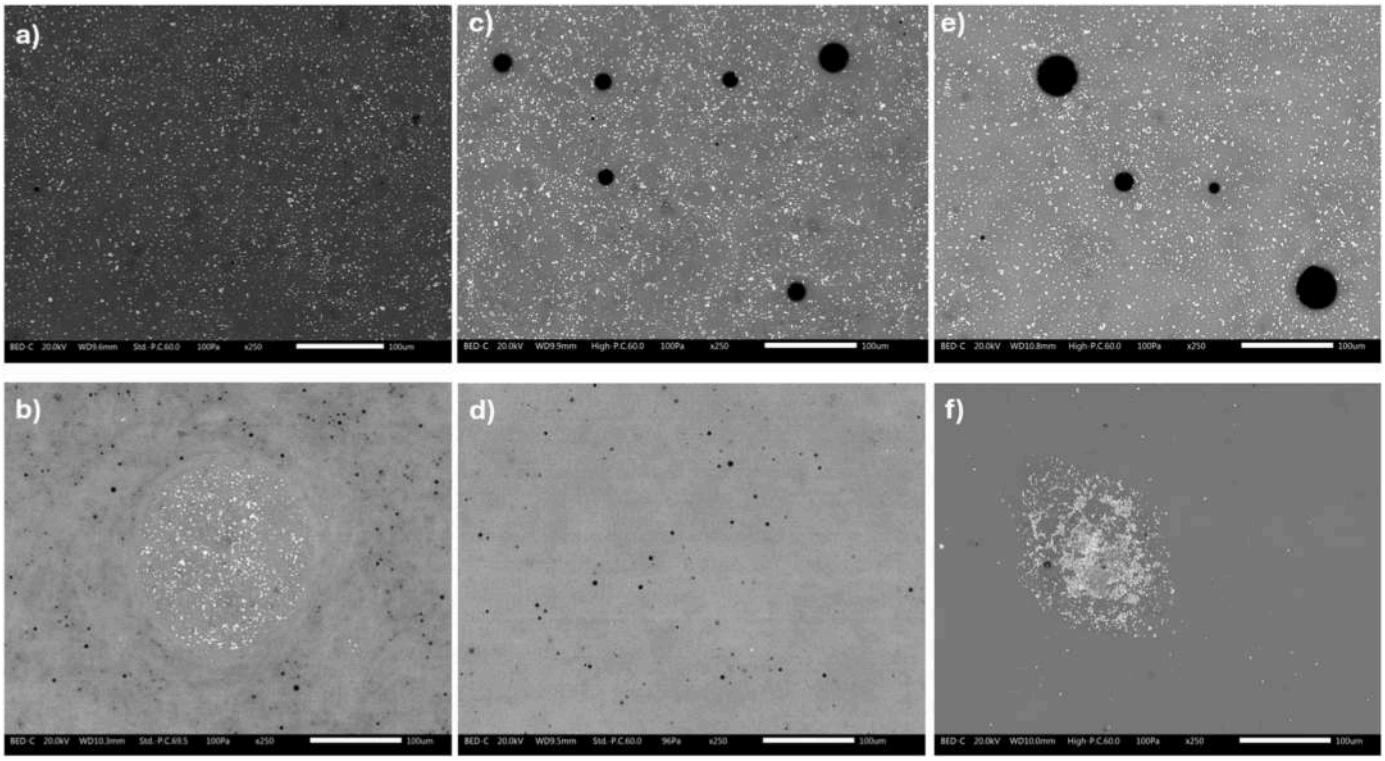

Figure 5. Surface images of the a) G1/40, b) T1/40, c) G2/40, d) T2/40, e) G2/80, and f) T2/80 using SEM/BED mode. Images were taken in BED mode.

12c). For Sample T2/40, the release of Co (Figure 12b) and Mn (Figure 12f) is reduced compared to T1/40. It is due to the full coverage

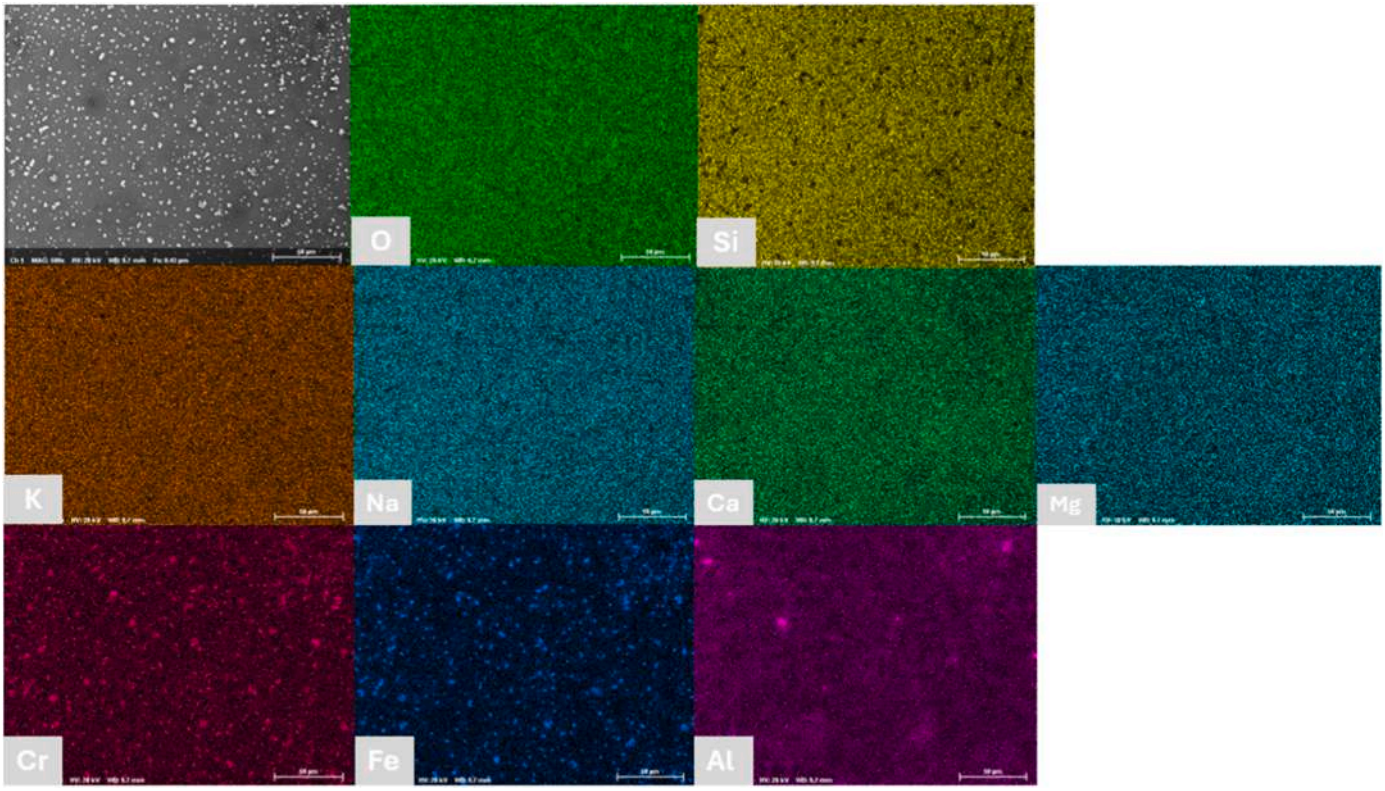

Figure 6. SEM image and associated EDS element mapping of G1/40.

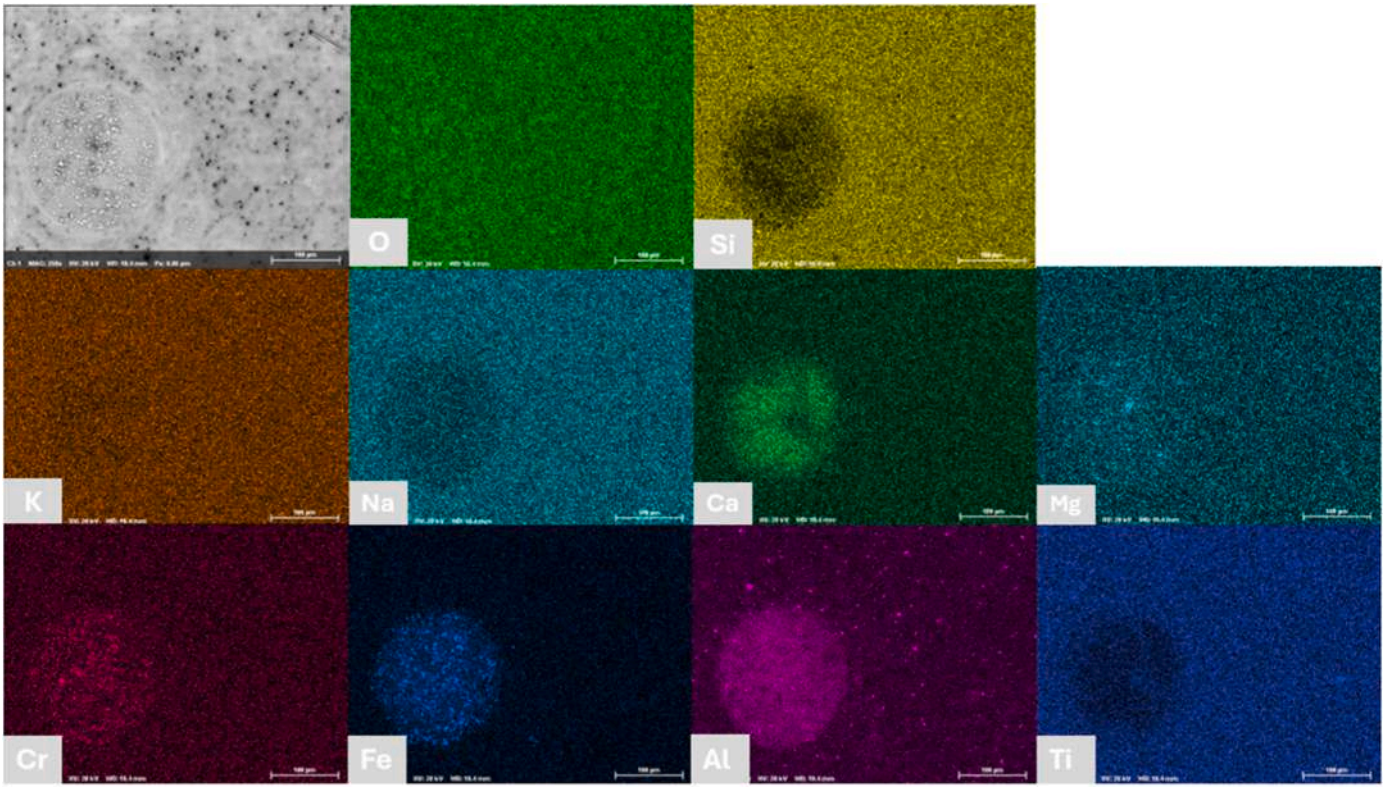

Figure 7. SEM image and associated EDS element mapping of T1/40.

of the ground layer, consistent with SEM results. This indicates that the top layer effectively limits the release of hazardous transition elements. However, it facilitates structural degradation of the network since Na and Si also leached after exposure (Figures 12g and 12h). At the higher firing temperature (Samples G2/80 and T2/80), the G2/80 maintains its stability with almost no alkali leaching. The application of the top layer

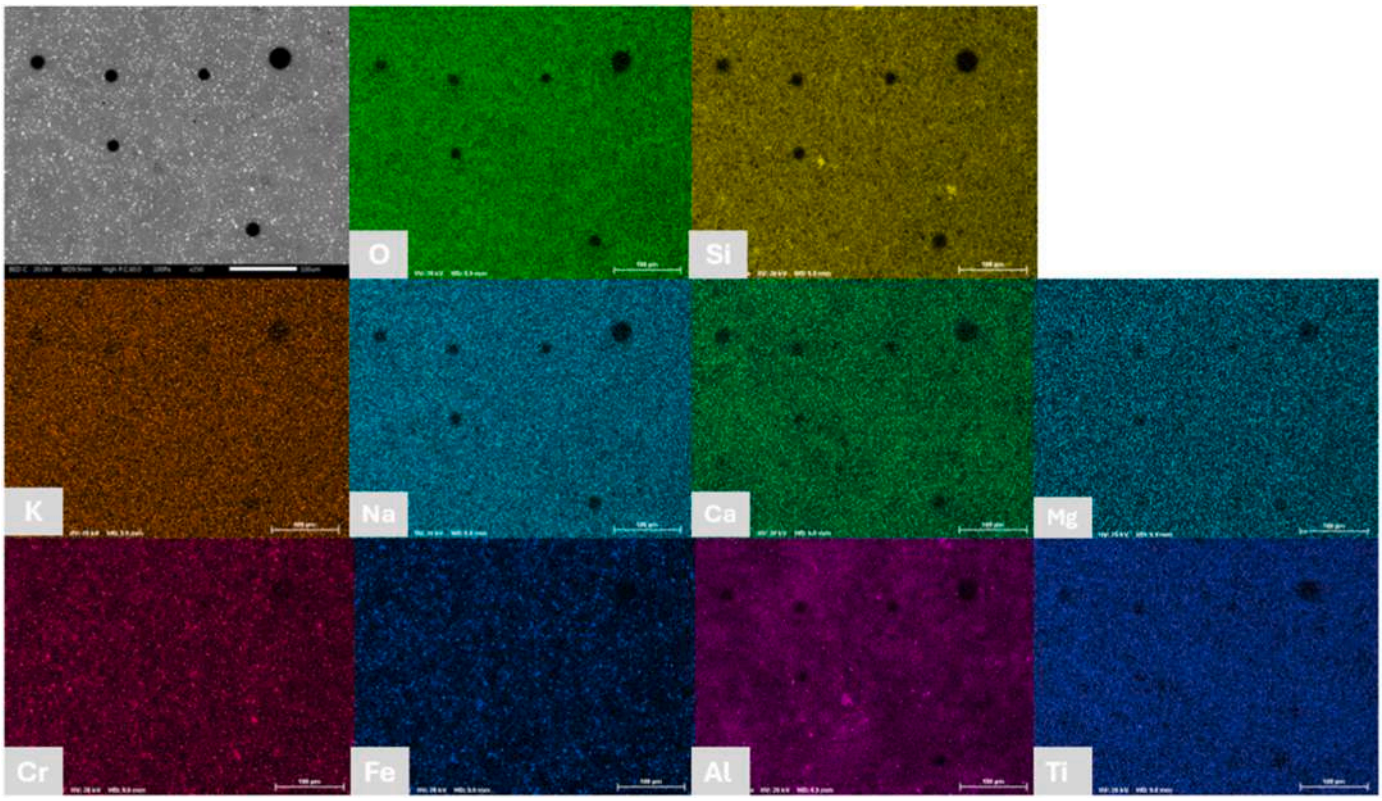

Figure 8. SEM image and associated EDS element mapping of G2/40.

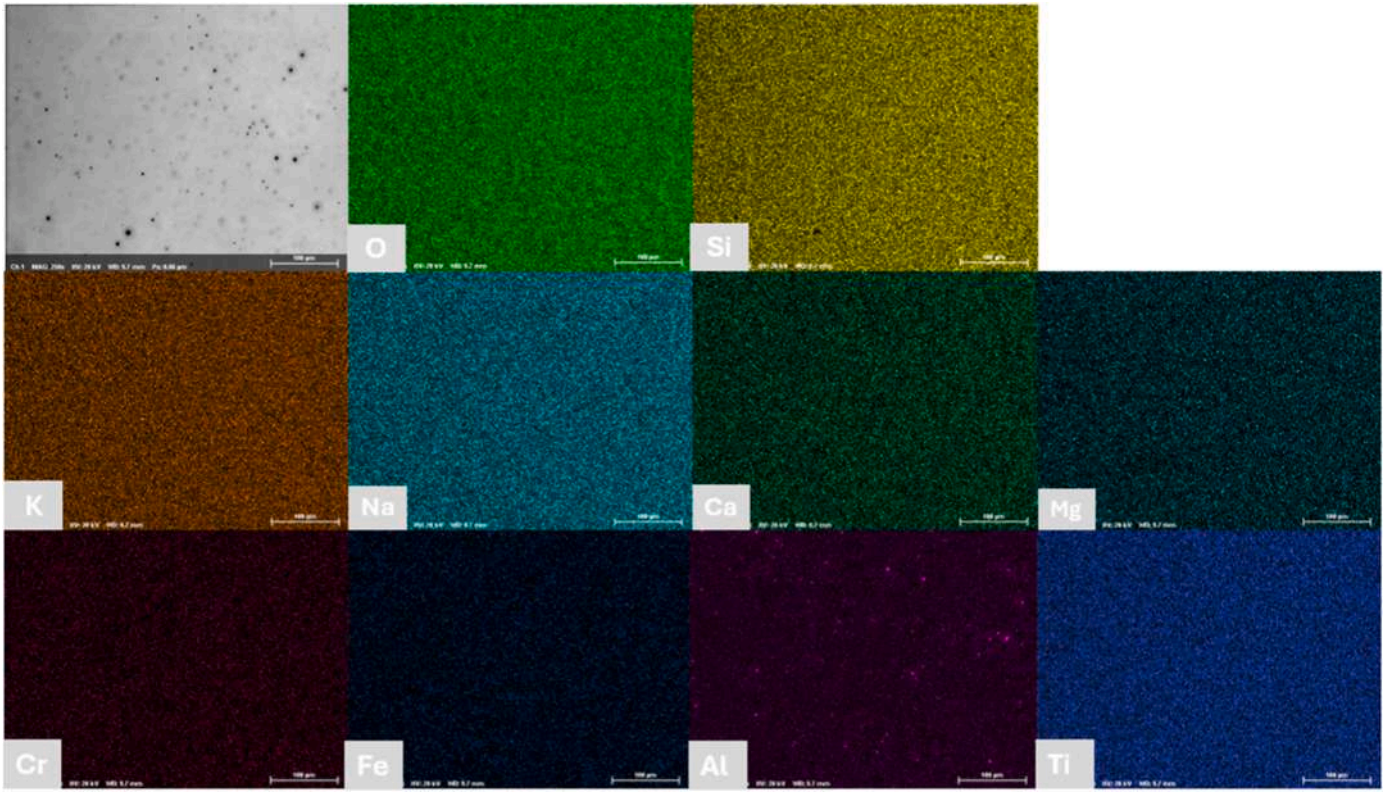

Figure 9. SEM image and associated EDS element mapping of T2/40.

(T2/80) causes a sharp release of Na and K (Figures 12g and 12d) within the first 2 days. However, a beneficial effect of the firing temperature is observed, since the release of these elements is lower than in the layer treated at a lower temperature. This rapidly decreases to much lower

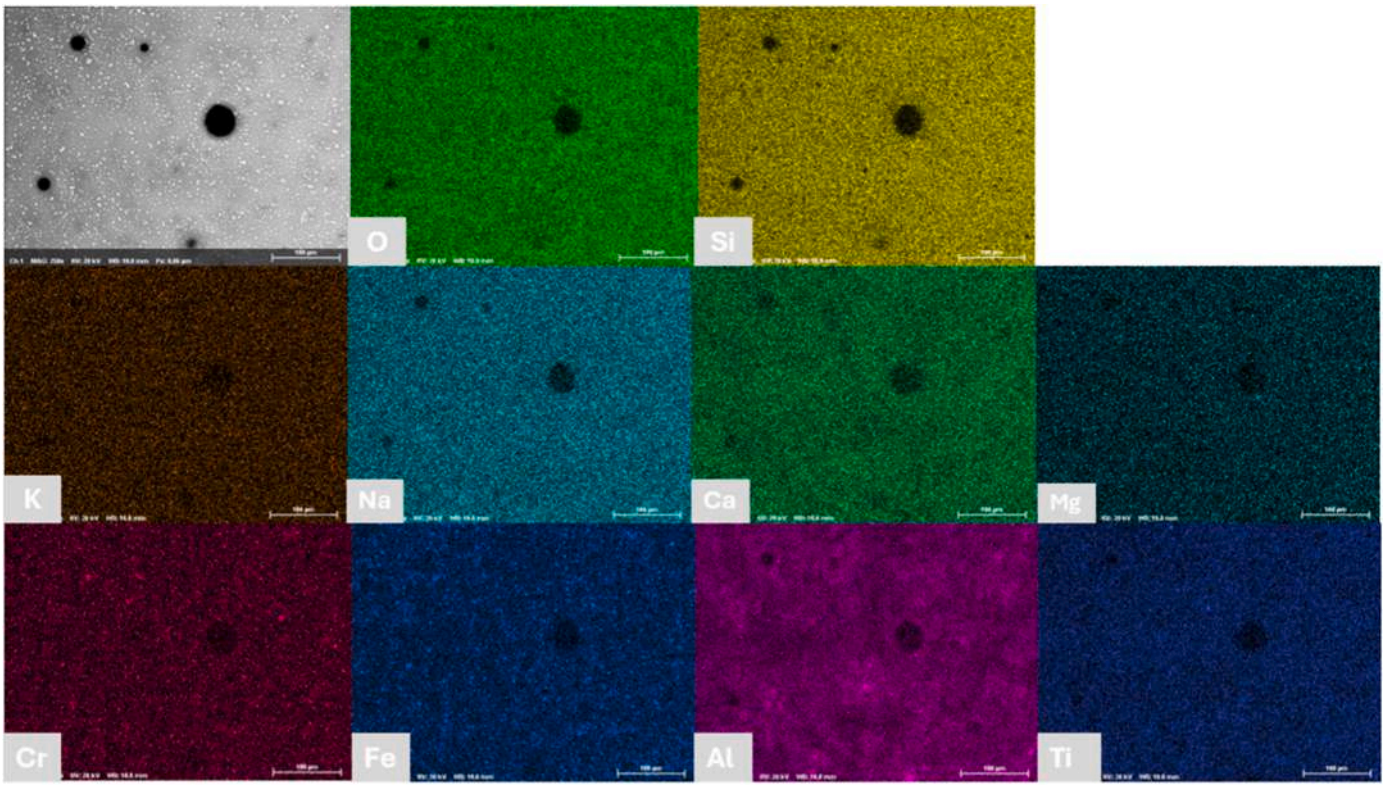

Figure 10. SEM image and associated EDS element mapping of G2/80.

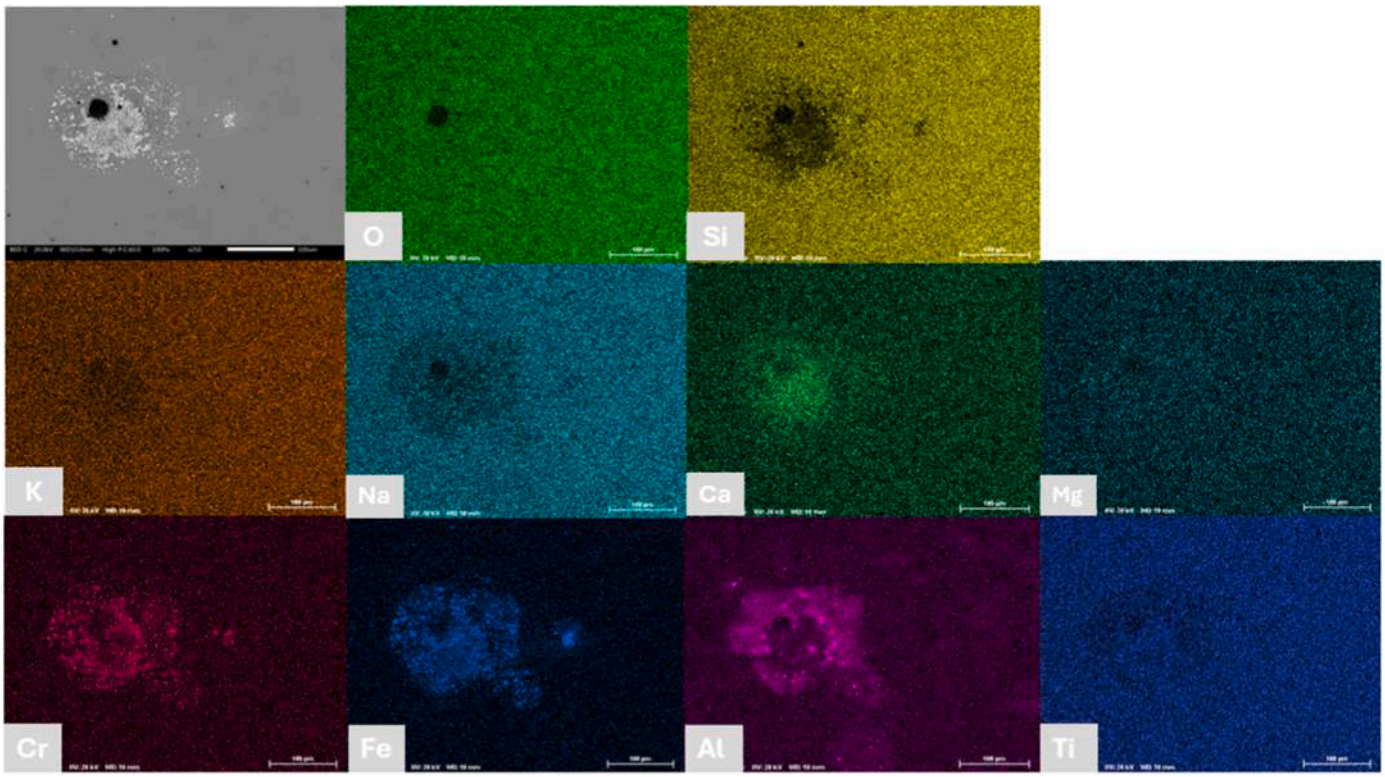

Figure 11. SEM image and associated EDS element mapping of T2/80.

levels as exposure time increases, suggesting that the microstructure developed at higher firing temperatures enhances the enamel's barrier effect and reduces long-term leaching. The higher temperature during the thermal treatment results in increased fluidity and enhanced spreading of the layer, which promotes more uniform and complete surface coverage. When examining Zn (Figure 12i) leaching, the highest

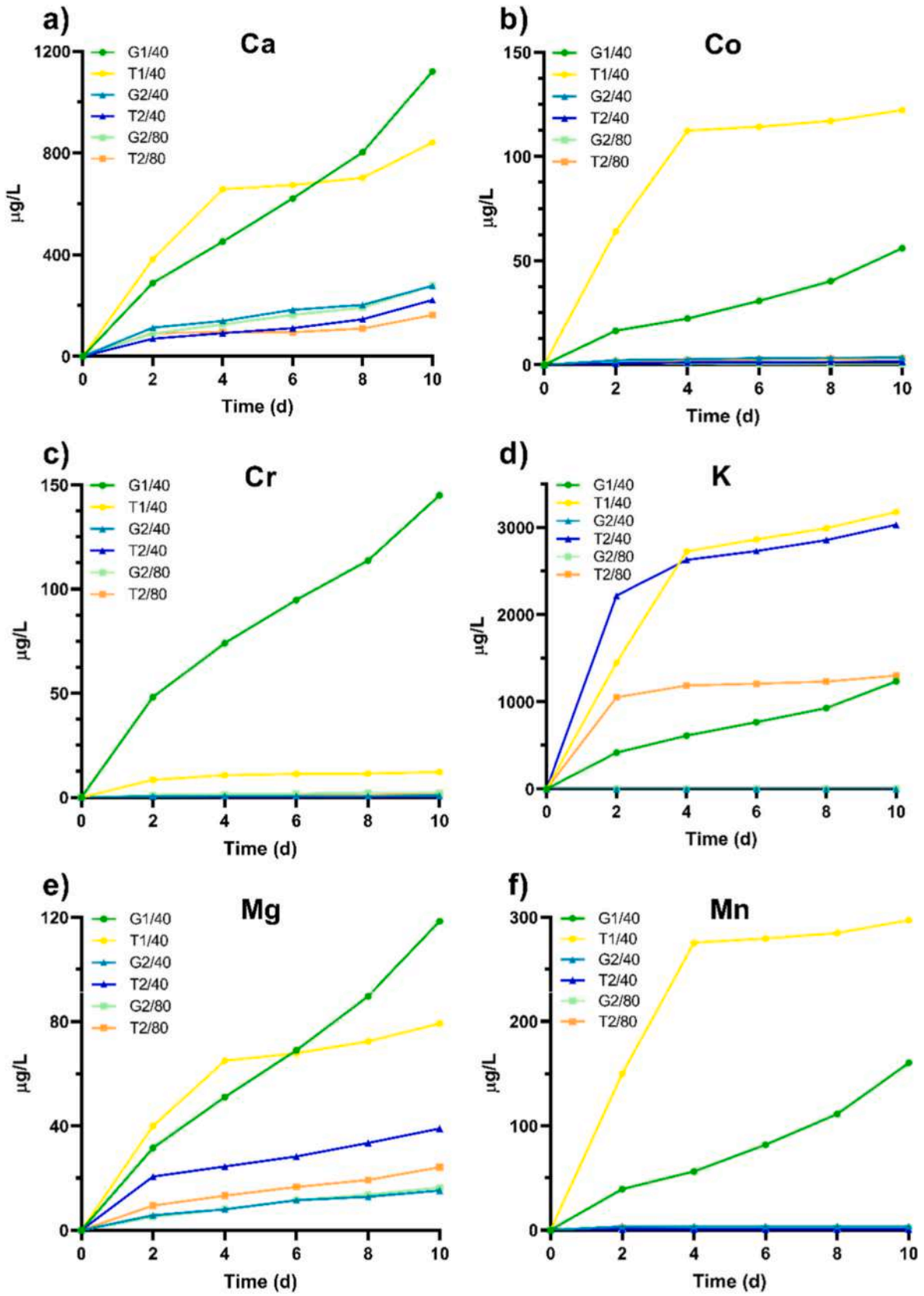

Figure 12. Trends of elements released (µg/L) over time a) Ca, b) Co, c) Cr, d) K, e) Mg, f) Mn, g) Na, h) Si, i) Zn, j) Li for all samples.

leaching occurs in T2/40, followed by T2/80, and then T1/40. This indicates that both temperature and coverage of the top layer on the ground coating are significant factors influencing the leaching process.

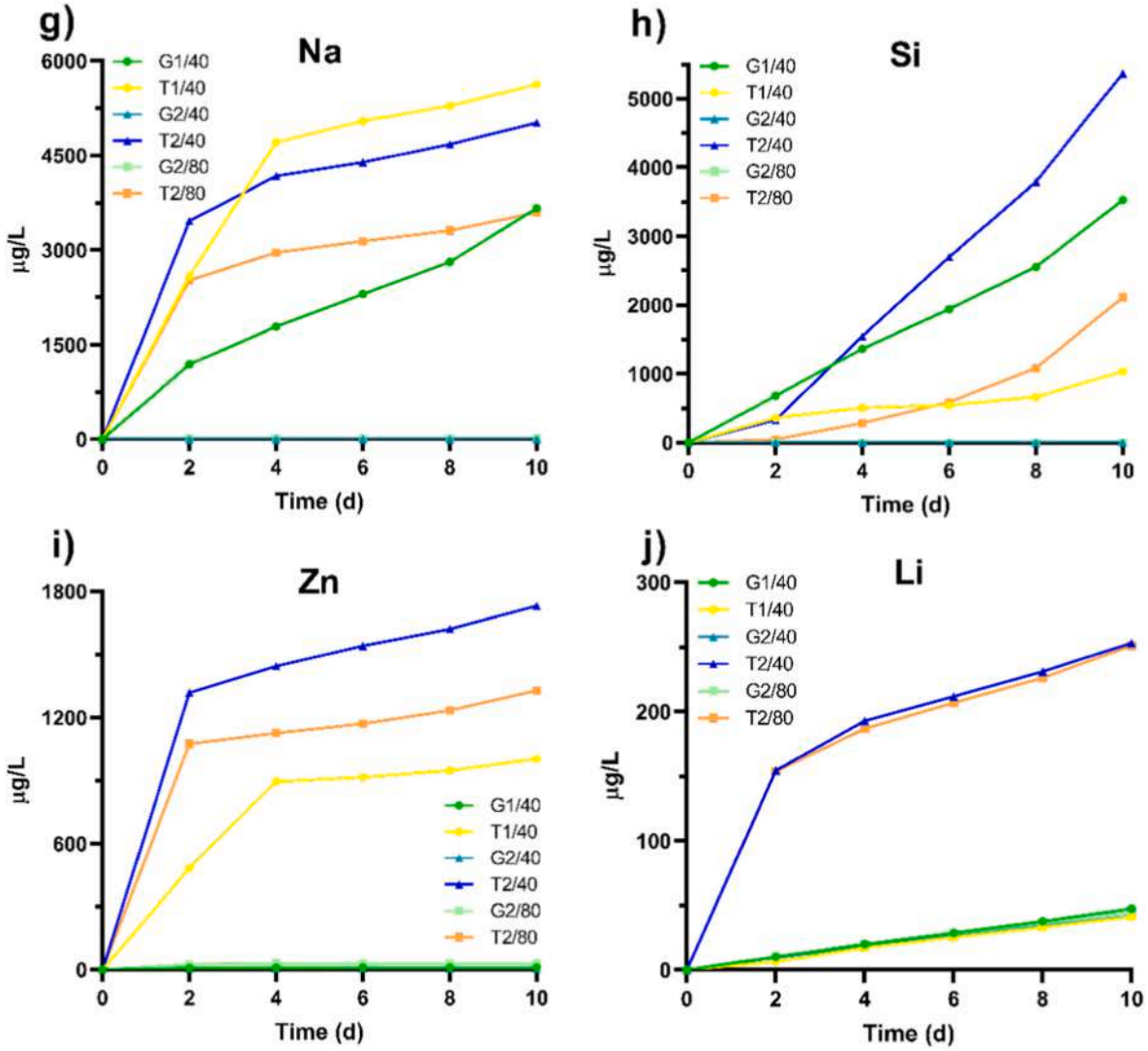

Figure 12. (*continued*).

3.3. Roughness analysis after exposing the distilled water

The surface roughness parameters (Ra and Rz) of the enamel coatings before and after exposure to distilled water are shown in Figure 13. For G1/40, both Ra and Rz slightly increase during exposure, indicating surface deterioration. T1/40 maintains a constant Ra after exposure and shows a small increase in Rz, likely due to localized degradation in some areas. Similarly, G2/40 displays only a slight increase in both parameters, demonstrating good chemical stability. However, for the T2/40 sample, the initial Ra is very low, and it increases significantly after exposure, with Rz rising sharply as well. This suggests that, despite its initially smooth surface, the coating becomes significantly rougher after leaching, indicating surface degradation. At the higher temperature (780 °C), G2/80 shows a slight reduction in Ra and Rz after exposure, implying that the coating retains its smoothness. The microstructure at this temperature was already rougher before testing, and the exposed area was rougher than the unexposed area. In contrast, T2/80 experiences a marked increase in both Ra and Rz, indicating severe surface roughening. This suggests that at higher temperatures, while the ground coating itself becomes more resistant, the top layer may lose its smoothness.

3.4. Microstructural analysis/investigation of enamel after exposure to distilled water

Figure 14 shows the microstructural images of the samples after exposure to distilled water. Figures 14a, 14c and, *14e* correspond to the ground coatings of G1 and G2, respectively. Considering G1/40 surface, localized attacks are observed, and it indicates that the fracture is mainly constrained to certain surface areas (Figure 14a). However, when the titanium-based enamel top layer is applied (T1/40), the crack density increases significantly. It becomes more widespread across the entire surface. Moreover, as shown in Figure 14b, the crack formation is more confined in regions where coarse Fe/Cr-rich particles are present, which are derived from the not totally covered ground layer. This behavior may be attributed to the local mismatches in thermal expansion. These uncovered areas act as stress concentrators and weak points during exposure to distilled water. By extracting some elements during contact with water, tensions can be created, which can lead to the nucleation of cracks. In G2/40, no visible cracks are detected (Figure 14c), confirming that G2 coating demonstrates superior chemical resistance to distilled water. When the titanium enamel top layer is applied (T2/40, Figure 14d), crack initiation and propagation occur. This is similar to what was observed in T1/40, with fractures spreading across the whole surface. Compared to T1/40, the surface of T2/40 is more extensively covered by the titanium enamel layer, as also shown in Figure 5.

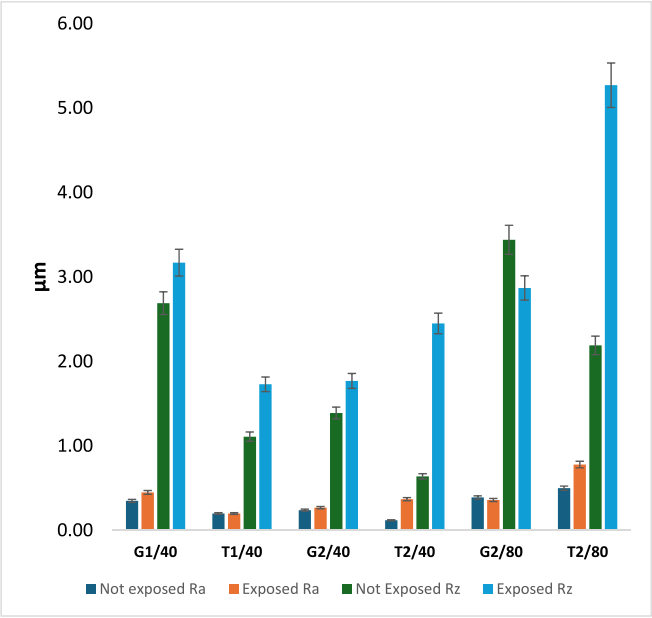

Figure 13. Results of surface Ra and Rz roughness before and after water exposure.

Therefore, the cracks are more widespread across the whole surface rather than local cracks. At the higher processing temperature of 780 °C, G2/80 surface (Figure 14e) remains without crack formation, pronouncing the improved stability of G2. When the enamel top layer is applied (T2/80, Figure 14f), cracks reappear. Although the damage is less severe and less widespread, it is still observable compared to samples processed at 740 °C. Increasing the processing temperature from 740 °C to 780 °C significantly improves the resistance of the system to distilled water. The crack formation behavior was investigated in more detail through EDS analysis, and the corresponding images are provided below (Figures 15 to 20). This provides a comparative evaluation of the influence of different ground coatings, top layer application, and processing temperatures on the chemical resistance of enameled cast irons.

Figure 15 presents the EDS analysis of G1/40 after exposure to distilled water. The microstructural image shows a defect due to gas formation and its subsequent escape from the enamel structure. In addition to this defect, localized attacks are examined, confirming the susceptibility of the coating to aqueous attack. Pores are initiation sites that facilitate the degradation of the enamel layer, enhancing the propagation of the attack. The EDS analysis indicates a significant depletion of alkali elements in several areas, with Na showing the highest degree of leaching, followed by K. Leaching of Na significantly disrupts the local chemical stability of the glassy matrix. The removal of network modifiers reduces structural integrity and encourages the formation of cracks. The crack initiated by the selective attack on Na-rich regions and was accelerated by crack propagation under exposure to distilled water.

Figure 16 shows the EDS analysis of T1/40. The top coating exhibits Na leaching, followed by K, consistent with the observations in G1/40. The EDS results also indicate that Na leaching is widespread across the entire surface. However, the cracks are pronounced in the uncovered area, which consist of the Fe-Cr compounds along with Al. The leaching of K and Na becomes more pronounced in this zone.

Figure 17 shows the EDS analysis of G2/40. The EDS results also indicate that G2/40 remains unchanged after exposure to distilled water. Compared to G1, G2, the presence of Li_2O might enhance the chemical resistance of the coating. This improvement is attributed to the smaller ionic radius of lithium, which also reinforces the overall network structure. In addition, the existence of TiO_2 contributes to the stability and durability of the coating by network polymerization through Ti-O-Si bonds.

Figure 18 shows the EDS analysis of T2/40 after exposure to distilled water. The results demonstrate that Na is the most intensively leached element. Coarse Fe and Cr particles are observed less, and only minor traces of Al are identified. The absence of Fe-Cr compounds reduces the thermal mismatch effects, hence they do not act as localized stress

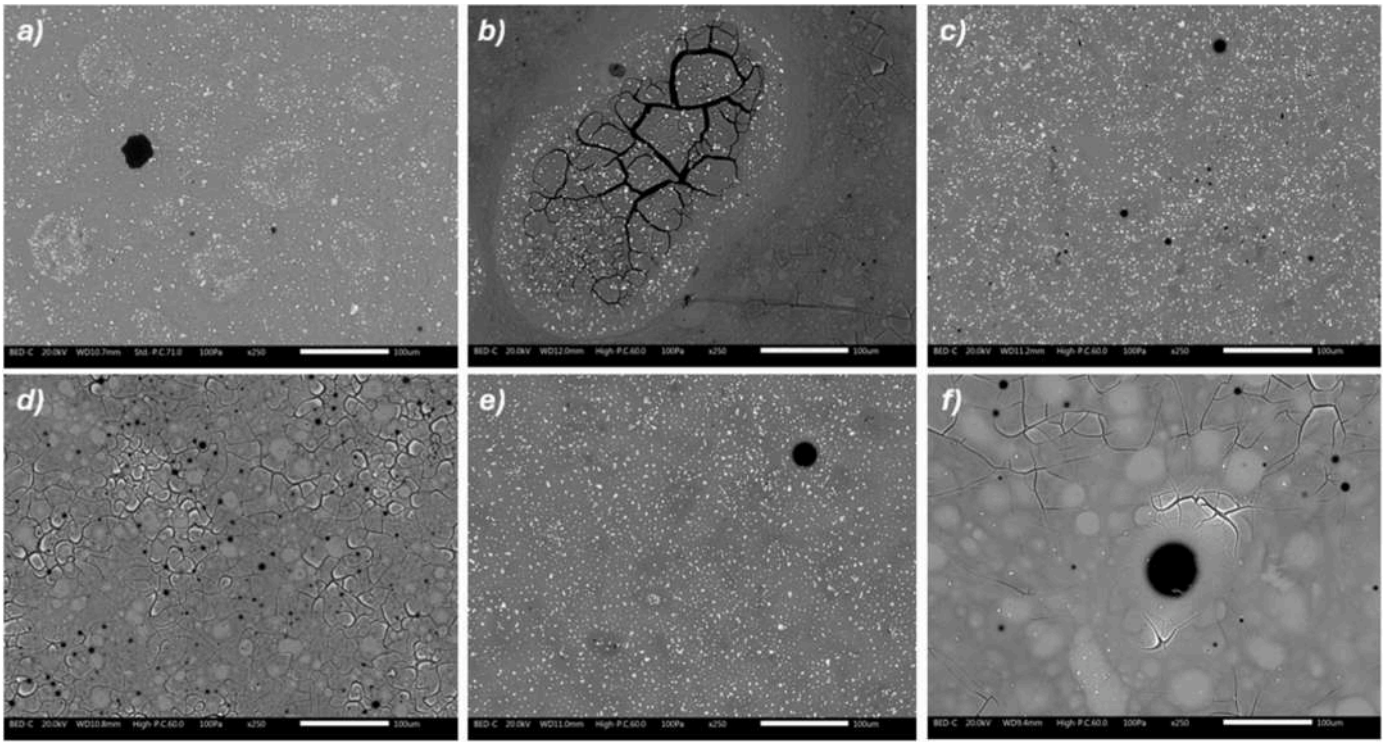

Figure 14. Surface images of the G1/40 (a), T1/40 (b), G2/40 (c), T2/40 (d), G2/80 (e) and, T2/80 (f) using SEM/BED mode after exposure to distilled water.

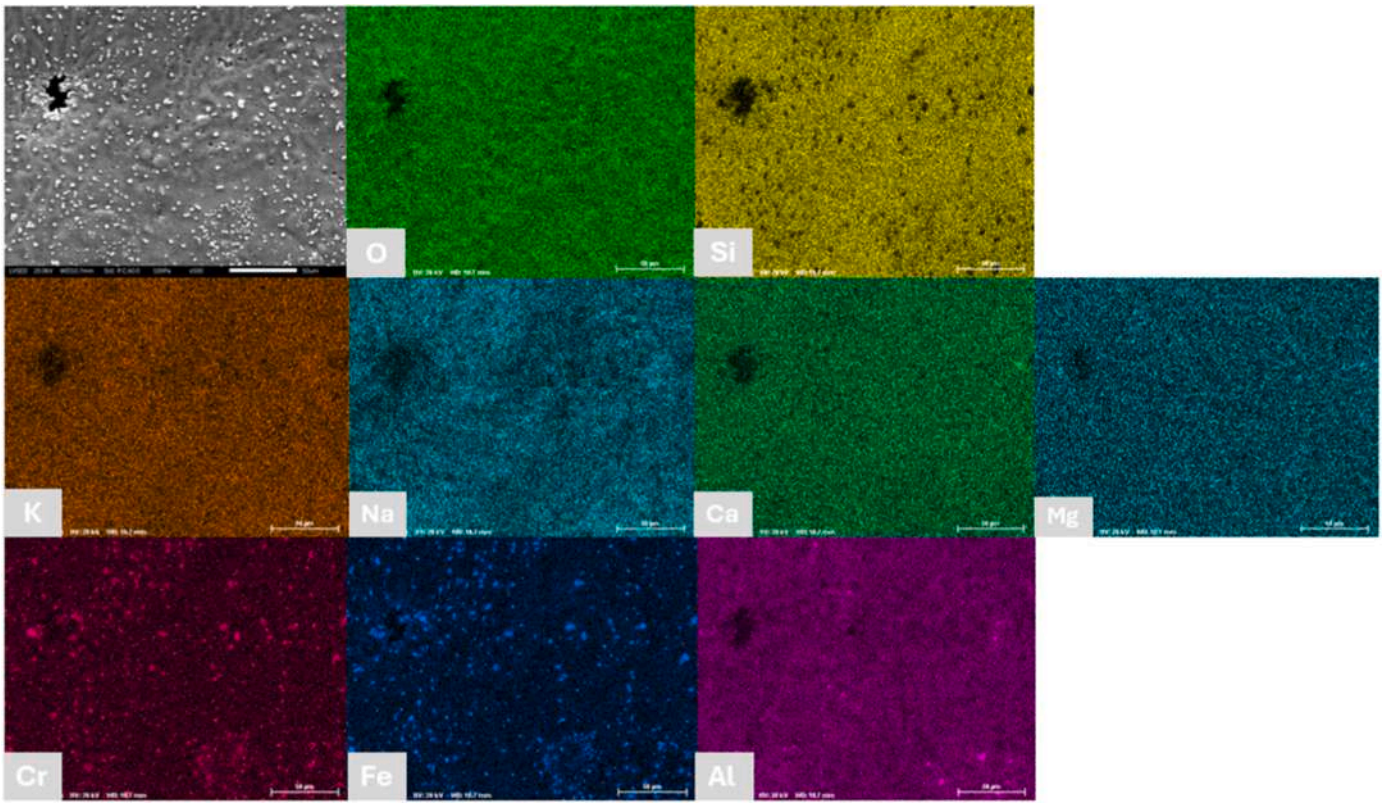

Figure 15. SEM image and associated EDS element mapping of G1/40 after exposure to distilled water.

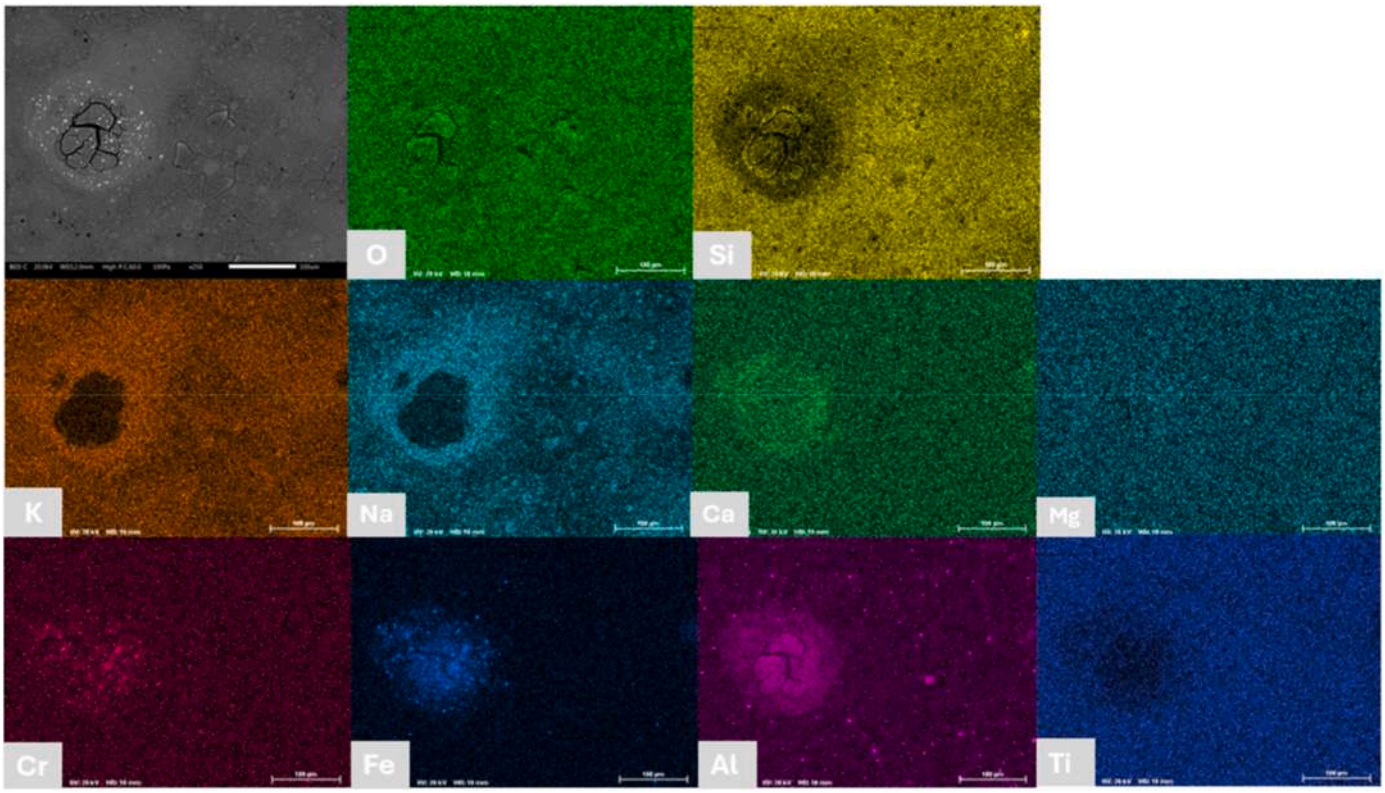

Figure 16. SEM image and associated EDS element mapping of T1/40 after exposure to distilled water.

concentrators. Therefore, fracture propagation is not limited to local areas, as observed in the ground coating.

Figure 19 presents the EDS mapping of G2/80 after exposure to water. Similar to G2/40, the structure remains unaffected by the

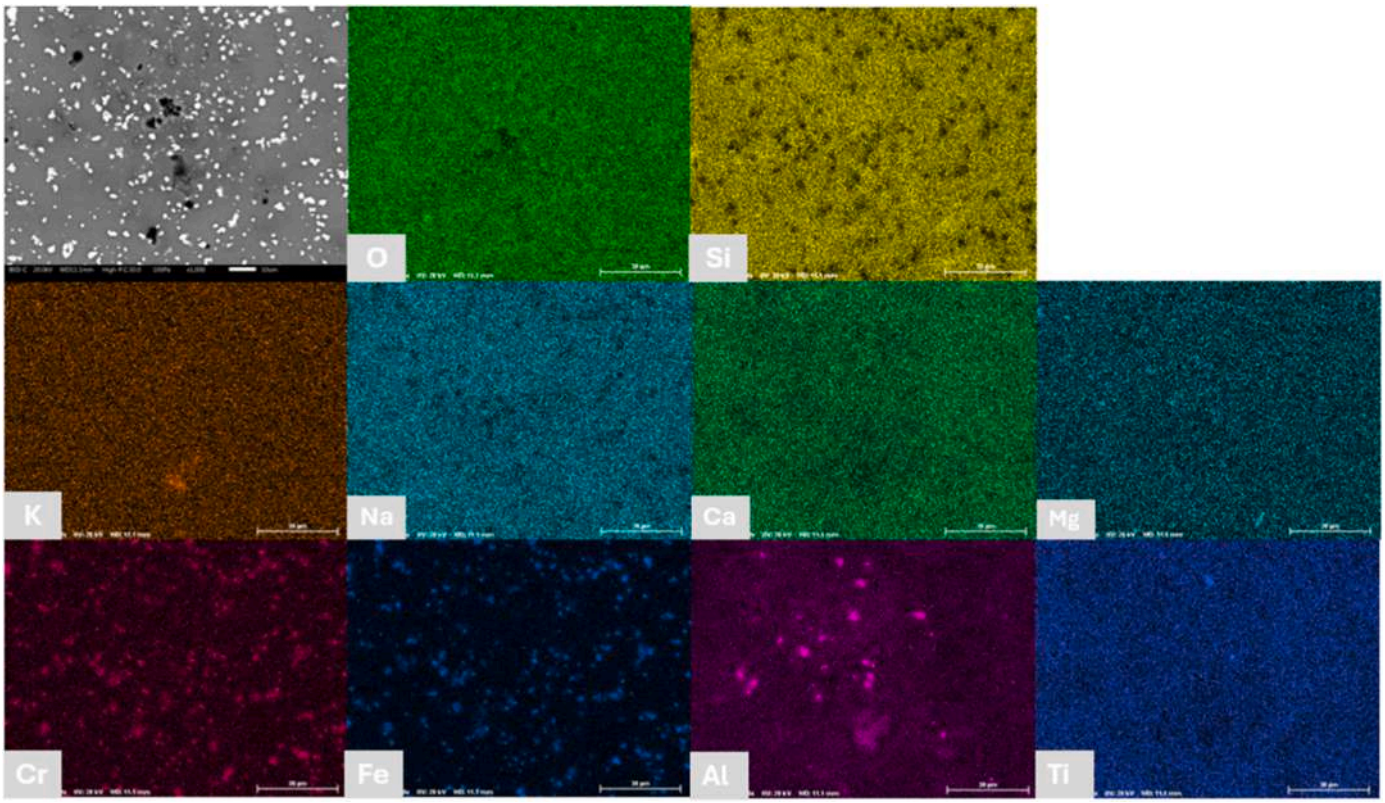

Figure 17. SEM image and associated EDS element mapping of G2/40 after exposure to distilled water.

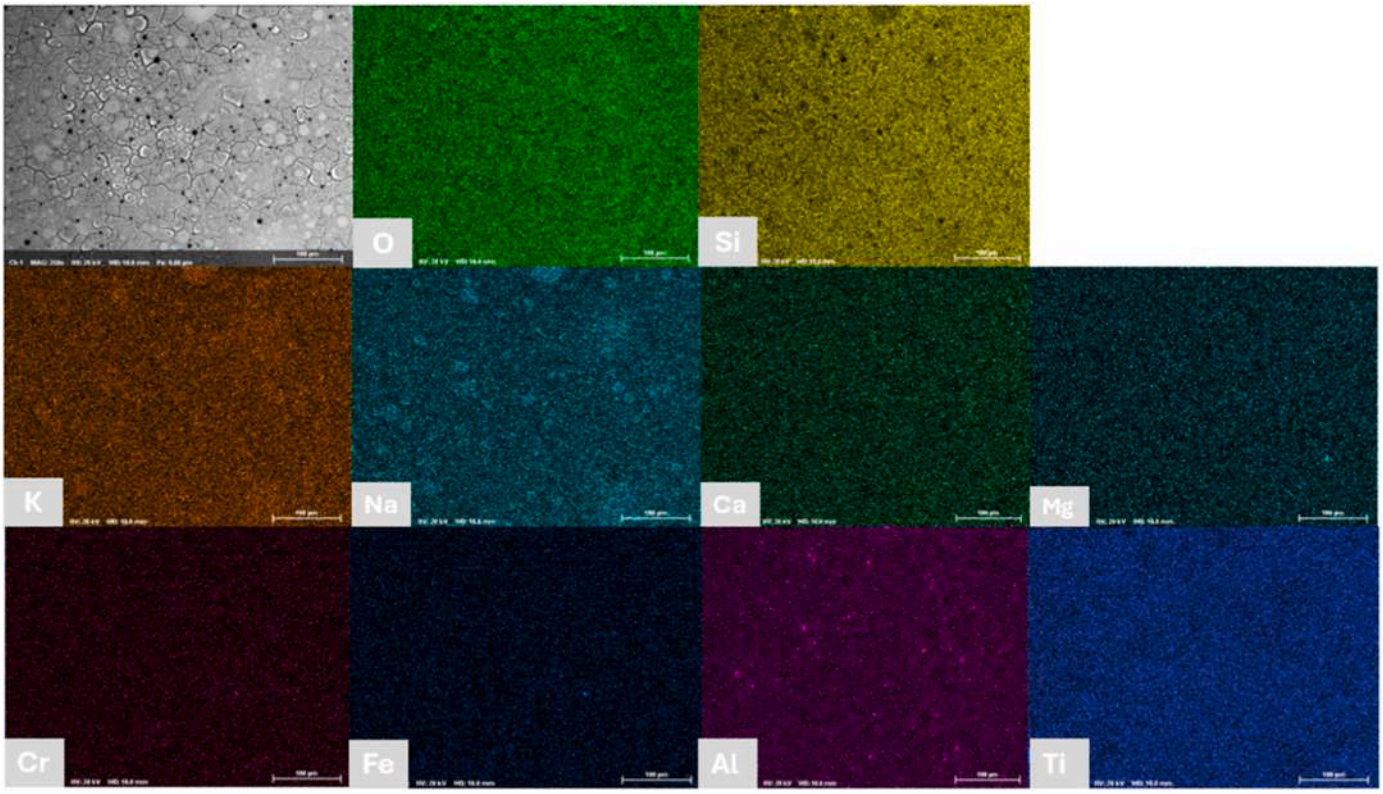

Figure 18. SEM image and associated EDS elemental mapping of T2/40 after exposure to distilled water.

distilled water. The observed defects are associated with gas formation and its subsequent release from the enamel structure. Additionally, regions with Al-containing particles are also observed. This behavior is due to the enhanced chemical resistance of the G2 composition, as

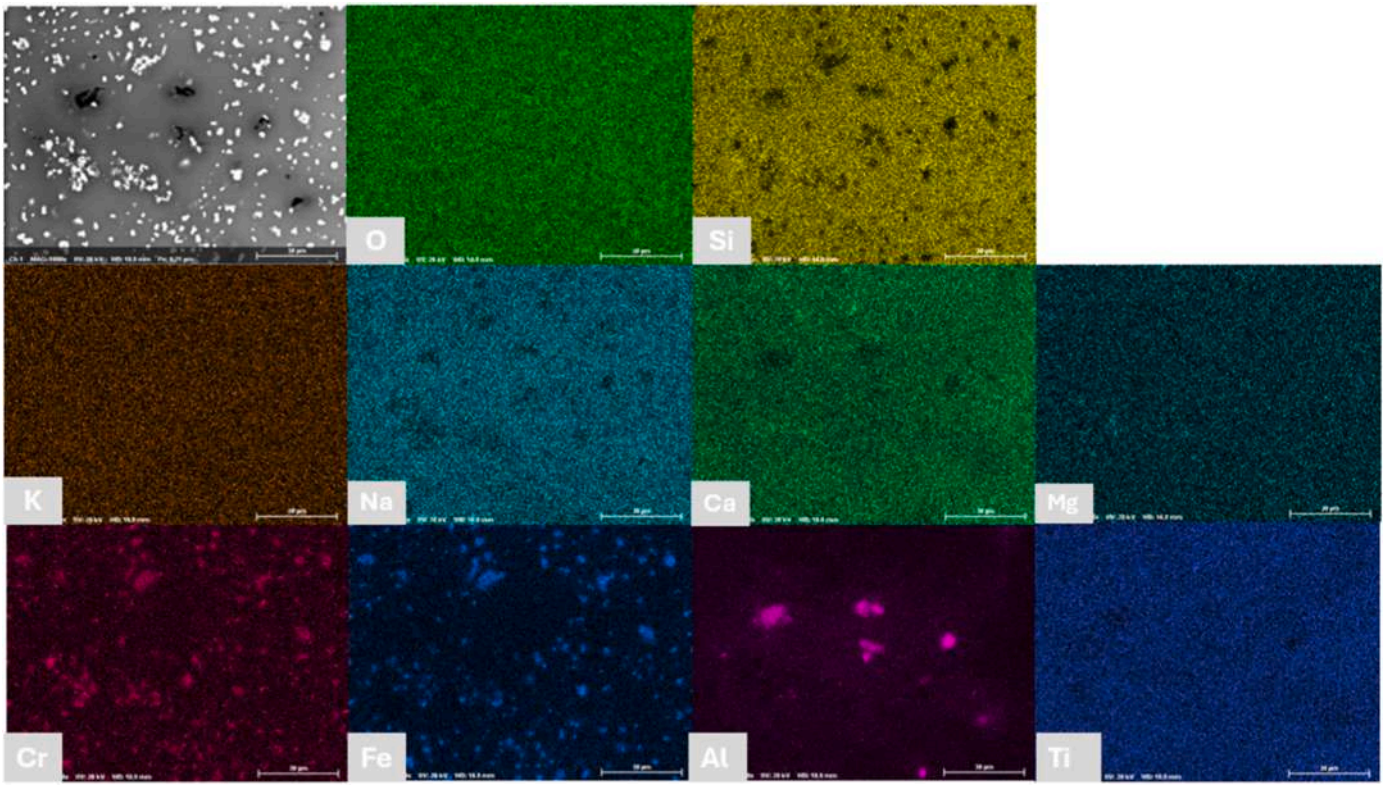

Figure 19. SEM image and associated EDS element mapping of G2/80 after exposure to distilled water.

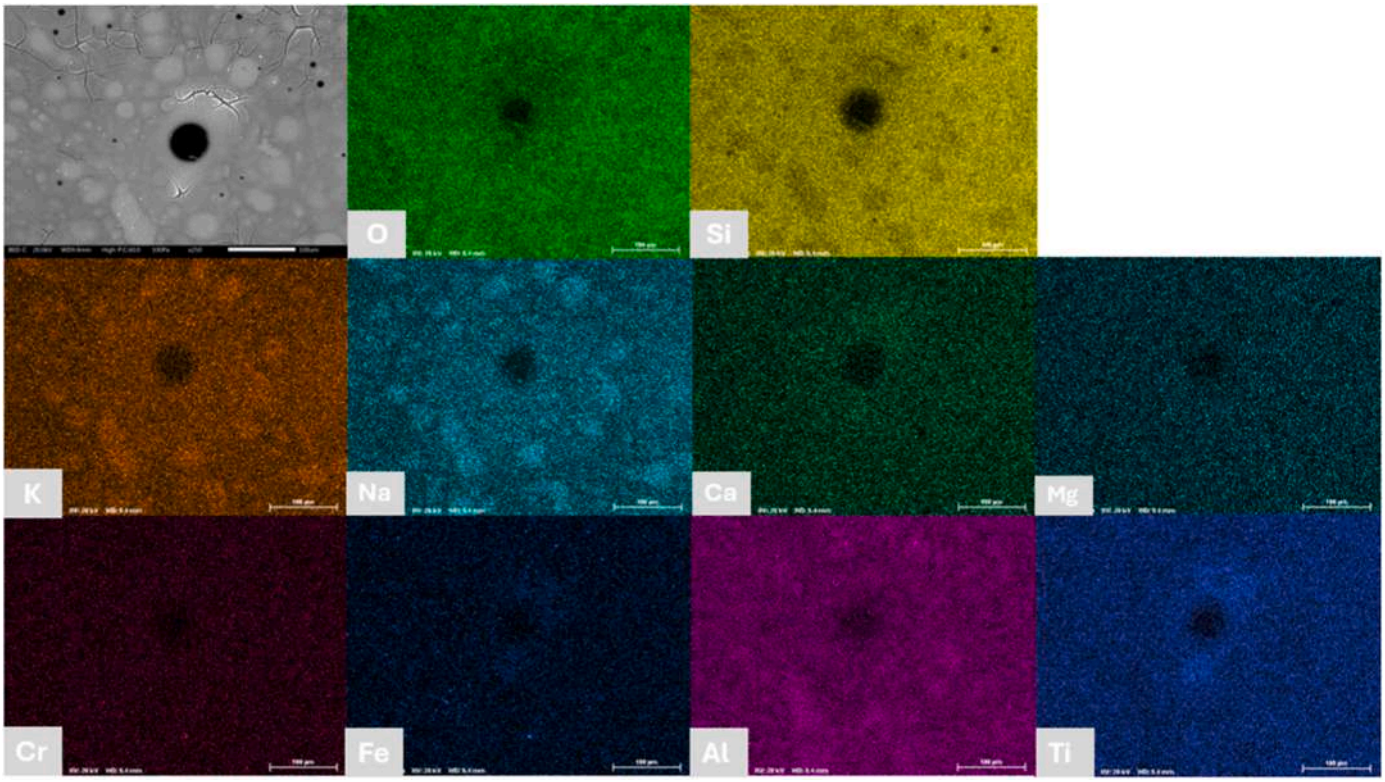

Figure 20. SEM image and associated EDS element mapping of T2/80 after exposure to distilled water.

previously commented.

Figure 20 shows the EDS analysis of T2/80 after exposure to distilled water with the top layer applied. The coating is affected by the dıstılled water, as cracks appear on the surface. These cracks primarily result from the leaching of Na and K, which act as network modifiers and weaken the glassy structure. In addition, regions of discoloration are

observed. Within these regions, Si is also depleted. This indicates that once Na and K are sufficient leached, the silica network itself susceptible vulnerable to dissolution. Interestingly, in the highly discolored zones, crack propagation tends to stop, suggesting a local stress relief associated with the breakdown of the glass network. Near the defective regions caused by gas release, Fe-rich compounds are detected, while Ti is largely absent.

In all samples, however, the very small size of the porosity in the top layer reduces the likelihood of forming preferential pathways for water to reach the substrate and leach potentially hazardous elements. Furthermore, the importance of the top layer thickness in achieving complete coverage of the ground layer was emphasized. The thicker T2/40 sample showed no exposed ground areas, thereby preventing water contact and reducing the extraction of Me and Co compared to the T1/40 sample.

Figure 21 shows cross-sectional images of the samples after water exposure. By comparing these microstructures with those of the samples before exposure, no significant reduction in coating thickness is observed. The extraction of elements and the associated degradation processes mainly affect the outermost layers of the coating. No defects, cracks, or open porosity are detected that could allow direct contact between the external environment and the substrate, which is crucial for maintaining corrosion protection. Therefore, for samples consisting only of ground layers, the coating thickness does not appear to be a determining factor. In contrast, for samples with an additional top layer, the thickness of the outer layer is critical not in terms of corrosion protection, but due to the difficulty of achieving complete coverage of the underlying ground layer. As shown in Figures 14b and 16, water-induced degradation is evident in the areas where the ground layer remains exposed. This effect is also clearly visible in Figure 21b.

Conclusions

This study examined the durability of enameled coatings on cast iron, made from a SiO_2-Na_2O-B_2O_3-CaO-Al_2O_3-based frit, after 10 days of exposure to distilled water, focusing on their compositional stability and microstructural changes. The results indicate that both the ground composition and the glaze top layer play crucial roles in determining the enamel's chemical durability, morphology, and overall performance. G2-based coatings demonstrated superior chemical resistance than G1-based coatings, mainly because of the addition of Li_2O and TiO_2, which increase the structural density. This enhancement resulted in improved resistance to distilled water and reduced alkali leaching. Conversely, G1 coatings experienced localized surface attacks and significant Na and K leaching, resulting in microcracks and gradual deterioration of the glassy matrix. The application of a titanium white top layer significantly improved surface smoothness and decreased the release of harmful transition elements like Cr, Mn, and Co. However, SEM observations showed limited surface dissolution and localized leaching, mostly around pores and areas with incomplete glaze coverage. ICP analysis confirmed that the G2-based samples (G2/40 and G2/80) remained highly stable, with almost no Na, K, or Si released. In contrast, applying the top layer induced initial alkali leaching, which stabilized over time. Surface roughness analysis showed that while roughness decreased after initial exposure, it increased after prolonged immersion due to localized attacks.

The presence of small-sized porosity in the top layer limits the formation of preferential pathways that could allow contact between the electrolyte and the underlying ground layers.

Future research could investigate long-term immersion tests and the relationship between chemical composition and leaching to further improve performance under specific environmental conditions.

The thickness of the top layer plays a fundamental role in ensuring complete coverage of the ground layer. Samples with a thickness greater than T2/40 showed no exposed ground. One possible approach, therefore, would be to adjust the top layer application parameters to increase the coating thickness and reduce or eliminate areas of exposed ground.

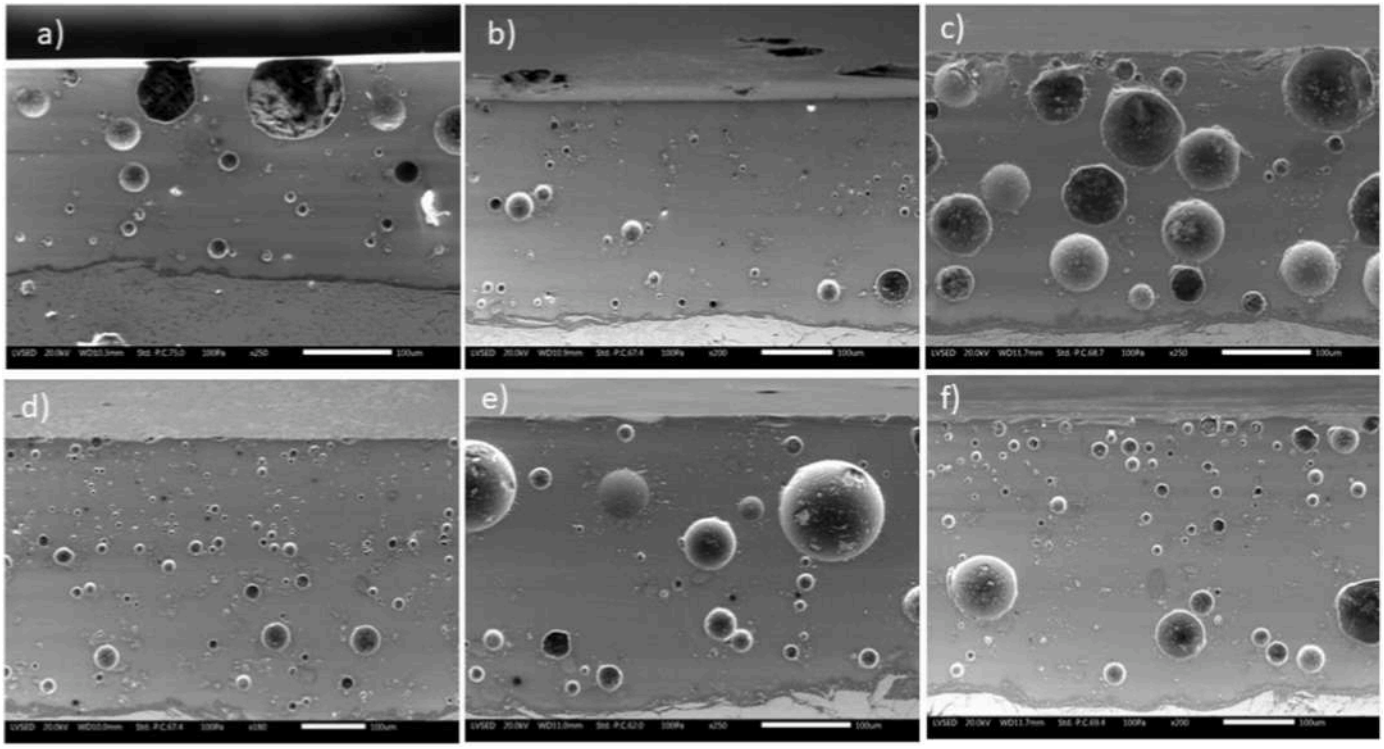

Figure 21. Cross section images of the G1/40 (a), T1/40 (b), G2/40 (c), T2/40 (d), G2/80 (e) and, T2/80 (f) using SEM/SE mode after exposure to distilled water. The samples were slightly tilted (5°) in order to allow observation of both the cross-section and the surface.

CRediT authorship contribution statement

Büşra Karakaş: Writing – review & editing, Writing – original draft, Visualization, Investigation, Formal analysis, Data curation. **Nicolò Mattei:** Writing – review & editing, Validation, Methodology, Conceptualization. **Luca Benedetti:** Writing – review & editing, Visualization, Investigation, Formal analysis, Data curation. **Stefano Rossi:** Writing – review & editing, Writing – original draft, Validation, Supervision, Project administration, Methodology, Funding acquisition, Formal analysis, Conceptualization.

Declaration of Competing interest

The authors declare that they have no known competing financial interests or personal relationships that could have appeared to influence the work reported in this paper.

Acknowledgment

The authors would like to thank Emaylum Italia, Chignolo d'Isola (BG), for kindly supplying the enameled samples and providing useful discussions.

References

[1] C. Nyby, et al., Electrochemical metrics for corrosion resistant alloys, Sci. Data 8 (1) (2021) 1–11, https://doi.org/10.1038/S41597-021-00840-Y.
[2] M. Iannuzzi, G.S. Frankel, The carbon footprint of steel corrosion, Npj Mater. Degrad. 6 (2022) 1–4, https://doi.org/10.1038/S41529-022-00318-1.
[3] D. Yan, Z. Xu, H. Qian, F. Tang, Y. Liu, Z. Huang, Phase structure and corrosion resistance of multilayer low-temperature sintered chemically reactive Enamel coatings, J. Mater.Civ. Eng. 32 (2020) 04020249, https://doi.org/10.1061/(Asce)Mt.1943-5533.0003334.
[4] D. Thomas, et al., Developments in smart organic coatings for anticorrosion applications: a review, Biomass Convers. Biorefin. 12 (2022) 4683–4699, https://doi.org/10.1007/S13399-022-02363-X.
[5] J. Deng, et al., Corrosion behavior of refractory TiNbZrMoV high-entropy alloy coating in static lead-bismuth eutectic alloy: a novel design strategy Of LBE corrosion-resistant coating, Surf. Coat. Technol. 448 (2022) 128884, https://doi.org/10.1016/J.Surfcoat.2022.128884.
[6] G. Jena, J. Philip, A review on recent advances in graphene oxide-based composite coatings for anticorrosion applications, Prog. Org. Coat. 173 (2022) 107208, https://doi.org/10.1016/J.Porgcoat.2022.107208.
[7] Y. Li, et al., Corrosion characteristics and mechanisms of ceramic coatings in subcritical and supercritical aqueous systems,", Ceram. Int. 51 (2025) 19743–19760, https://doi.org/10.1016/J.Ceramint.2025.02.258.
[8] H. Kania, Corrosion and anticorrosion of Alloys/Metals: the important global issue,", Coatings 13 (2023) 216, https://doi.org/10.3390/Coatings13020216.
[9] S. Rossi, F. Russo, A.M. Compagnoni, A Brief History of Porcelain Enamel: from Artistic Enamel to Technical Enamelling, 2020, pp. 1–8, https://doi.org/10.32545/Encyclopedia202007.0019.V1.
[10] G. Yan, Y. Wu, W. Liu, W. Yu, S. Shen, Stress evolution In enamel Coating/Ni-Based alloy systems During isothermal oxidation, J Appl Phys 135 (2024) 85103, https://doi.org/10.1063/5.0185084/3266879.
[11] J.-C. Choi, S.-J. Park, H. Goh, J.Y. Lee, M.O. Eom, M. Kim, A Study On migration of heavy metals From kitchen utensils including glassware, ceramics, Enamel, earthenware and plastics, J. Fd Hyg. Safety 29 (2014) 334–339, https://doi.org/10.13103/Jfhs.2014.29.4.334.
[12] A. Lejeune, et al., Role Oo crystallization on the thermomechanical behavior of enamels used for automotive application, J. Eur. Ceram. Soc. 45 (2025) 117106, https://doi.org/10.1016/J.Jeurceramsoc.2024.117106.
[13] A. Zanardi, M. Calovi, S. Rossi, Porcelain enamel coatings for building façades, Appl. Sci. 13 (2023) 9952, https://doi.org/10.3390/App13179952.
[14] A.V. Ryabova, E.A. Yatsenko, L.V. Klimova, A.Y. Fanda, Development of a weld Enamel technology for the installation of steel pipelines with an internal Silicate-Enamel coating, Mater. Today Proc. 38 (2021) 1491–1494, https://doi.org/10.1016/J.Matpr.2020.08.135.
[15] V. Lobaz, et al., Low-Melting phosphate glass coatings for structural parts composed of depleted uranium, Coatings 12 (2022) 1540, https://doi.org/10.3390/Coatings12101540/S1.
[16] V.Y. Borovoy, O.V. Kazmina, V.V. Shekhovtsov, Induction synthesis of frit for Enamel coating of steel pipes,", Glass Ceram 80 (2023) 290–294, https://doi.org/10.1007/S10717-023-00600-X.
[17] D. Song, et al., Development of high-performance enamel coating on grey iron by low-temperature sintering,", Materials 11 (2018) 2183, https://doi.org/10.3390/Ma11112183.
[18] Y. Bao, D.T. Gawne, J. Gao, T. Zhang, B.D. Cuenca, A. Alberdi, Thermal-Spray deposition of Enamel on aluminium alloys, Surf Coat Technol 232 (2013) 150–158, https://doi.org/10.1016/J.Surfcoat.2013.04.065.
[19] F. Li, M. Chen, Q. Wang, F. Wang, Effect of Al_2O_3 content on microstructure and oxidation behavior of Silicate Enamel coatings on a Ni-Based superalloy at 1000 C, Ceram. Int. 48 (2022) 25445–25457, https://doi.org/10.1016/J.Ceramint.2022.05.222.
[20] Y. Xiong, S. Zhu, F. Wang, The oxidation behavior and mechanical performance of Ti60 alloy with Enamel coating, Surf. Coat. Technol. 190 (2005) 195–199, https://doi.org/10.1016/J.Surfcoat.2004.09.005.
[21] Y. Liao, et al., Thermal shock and self-healing behavior of the enamel composite coatings with addition of various nanoparticles at temperatures of 700 And 800 °C, Corros. Sci. 191 (2021) 109747, https://doi.org/10.1016/J.Corsci.2021.109747.
[22] P.G. Allison, R.D. Moser, C.A. Weiss, P.G. Malone, S.W. Morefield, Nanomechanical and chemical characterization of the interface Between concrete, glass–ceramic bonding enamel and reinforcing steel, Constr. Build. Mater. 37 (2012) 638–644, https://doi.org/10.1016/J.Conbuildmat.2012.07.066.
[23] Ronghai Xu, S. Xin, Q. Ni, H. Zeng, M. Li, Initial corrosion characteristics of Enamel coated carbon steel in hot tap water, Russ. J. Electrochem. 57 (2020) 636–643, https://doi.org/10.1134/S1023193520120265.
[24] I. Pavlovska, K. Malnieks, G. Mezinskis, L. Bidermanis, M. Karpe, Hard TiO_2–SiO_2 sol–gel coatings for Enamel against chemical corrosion, Surf. Coat. Technol. 258 (2014) 206–210, https://doi.org/10.1016/J.Surfcoat.2014.09.027.
[25] S. Rossi, C. Zanella, R. Sommerhuber, Influence of mill additives on vitreous enamel properties, Mater. Des. 55 (2014) 880–887, https://doi.org/10.1016/J.Matdes.2013.10.059.
[26] H. Wang, et al., Evaluation Of glass coatings with various Silica Content corrosion in a 0.5 M HCl water solution, Crystals 11 (2021) 346, https://doi.org/10.3390/Cryst11040346.
[27] A.S. Kassem, M.Z. Mostafa, M.F. Abadir, S.A. El Sherbiny, Hot water acid-resistant enamels for sheet steel, Mater. Corr. 61 (2010) 58–63, https://doi.org/10.1002/Maco.200805230.
[28] D.A. Izgagina, M.Y. Uglinskikh, S.G. Vlasova, Composition development and property Study of alkali-resistant enamel for the protection of chemical apparatus, Glass Ceram V75 (2018) 234–236, https://doi.org/10.1007/S10717-018-0062-1.
[29] A.V. Ryabova, E.A. Yatsenko, V.V. Kerimova, L.V. Klimova, A.Y. Fanda, V. A. Smolii, Glass enamel monolayer coating for the protection of steel articles against corrosion, Glass Phys. Chem. 45 (2019) 82–84, https://doi.org/10.1134/S1087659619010085.
[30] W. Li, H. Hong, X. Qu, C. Li, Y. Elena, Enamel coatings mill additives optimization for Sulfuric acid corrosion,", Int J Appl Ceram Technol 21 (2024) 1119–1131, https://doi.org/10.1111/Ijac.14538.
[31] F. Tang, H. Cui, Y. Kuang, G. Li, Z. Lin, Corrosion resistance and bond strength of Silica Particle Modified Enamel coated smooth and deformed steel bars, J. Mater. Civ. Eng. 36 (2024) 04024181, https://doi.org/10.1061/Jmcee7.Mteng-17288.
[32] E. Medvedovski, G. Leal Mendoza, Enamel (Glassy) coatings for steel protection against high temperature corrosion, Adv. Appl. Ceram. 122 (2023) 145–169, https://doi.org/10.1080/17436753.2023.2231699.
[33] G. Boissonnet, E. Rzad, R. Troncy, T. Dudziak, F. Pedraza, High temperature oxidation of Enamel coated low-alloyed steel 16Mo3 in water vapor, Coatings 13 (2023) 342, https://doi.org/10.3390/Coatings13020342.
[34] K. Chen, et al., Corrosion of SiO_2–B_2O_3–Al_2O_3–CaF_2-R_2O (R=Na And K) enamels with different content Of ZrO_2 In H_2SO_4 and NaOH solutions, Ceram. Int. 45 (2019) 14958–14967, https://doi.org/10.1016/J.Ceramint.2019.04.232.
[35] X. Zhang, et al., Effect of zirconium diboride on mechanical properties and alkali corrosion resistance of Enamel, Int J Appl Ceram Technol 22 (2025) 15170, https://doi.org/10.1111/ijac.15170.
[36] F. Tang, Y. Kuang, H. Cui, Z. Lin, Corrosion and bond behavior of Silicate Dioxide Particle modified Enamel coated steel bar, in: Life-Cycle of Structures and Infrastructure Systems - Proceedings of the 8th International Symposium on Life-Cycle Civil Engineering, Ialcce, 2023, p. 2911, https://doi.org/10.1201/9781003323020-354, 2908.
[37] L. Fan, F. Tang, G. Chen, S.T. Reis, M.L. Koenigstein, Corrosion resistances of steel pipe coated with two types of Enamel by two coating processes, J. Mater. Eng. Perform. 27 (2018) 5341–5349, https://doi.org/10.1007/S11665-018-3656-4.
[38] Y.L. Li, Z.R. Huang, Q.D. Zhong, C. Chen, Y.X. Xu, CECM applied for researching the microscopic morphology and corrosion behavior of Enamel coating on mild steel in aqueous chloride solutions, Surf. Rev. Lett. 25 (2018) 1–8, https://doi.org/10.1142/S0218625x18500944. Jul. 2018.
[39] D. Yan, S. Ye, H. Qian, P. Guo, Y. Liu, Chemical resistance and corrosion mechanism of aluminophosphate-based Low Temperature Enamel (LTE) in H_2SO_4 and NaOH solutions, Ceram. Int. 50 (2024) 19709–19719, https://doi.org/10.1016/J.Ceramint.2024.03.095.
[40] S. Rossi, M. Fedel, L. Da Col, F. Deflorian, S. Petrolli, Coatings to increase the corrosion behaviour of aluminium foam, Surf. Eng. 33 (2017) 405–409, https://doi.org/10.1080/02670844.2016.1276700.
[41] L. Fan, S.T. Reis, G. Chen, M.L. Koenigstein, Corrosion resistance of pipeline steel with damaged enamel coating and cathodic protection, Coatings 8 (2018) 185, https://doi.org/10.3390/Coatings8050185.
[42] H.M. Hussein Farh, M.E.A. Ben Seghier, R. Taiwo, T. Zayed, Analysis and ranking of corrosion causes for water pipelines: a critical review, Npj Clean Water 6 (2023) 1–17, https://doi.org/10.1038/S41545-023-00275-5.
[43] Q. Hu, et al., Mechanisms of corrosion and corrosion Scale Formation in water supply networks: a review, J. Water Process Eng. 75 (2025) 107975, https://doi.org/10.1016/J.Jwpe.2025.107975.

[44] G.A. Cox, B.A. Ford, The long-term corrosion of glass by ground-water, J. Mater. Sci. 28 (1993) 5637–5647, https://doi.org/10.1007/Bf00367840.
[45] J. Hu, et al., Impacts of water quality on the corrosion of cast iron pipes for water distribution and proposed source water switch strategy, Water Research 129 (2018) 428–435, https://doi.org/10.1016/j.watres.2017.10.065.
[46] Holger Evele, Peter Vodak, William D. Faust, Cast Iron Process Control in a developing Market, 69th Porcelain Enamel Institute Technical Forum: Ceramic Engineering And Science Proceedings 28 (10) (2007) 19–22, https://doi.org/10.1002/9780470614488.Ch4.
[47] N. Mattei, L. Benedetti, S. Rossi, Corrosion behavior of porcelain enamels in water tank storage, Coatings 15 (2025) 934, https://doi.org/10.3390/Coatings15080934.
[48] P.G. Pauksh, Some problems with enamelling cast-iron articles, Glass Ceram. 49 (1992) 241–248, https://doi.org/10.1007/Bf00676942/Metrics.
[49] S. Papavinasam, Materials, in: Corrosion Control in the Oil and Gas Industry, Elsevier, Amsterdam NL, 2014, pp. 133–177, https://doi.org/10.1016/B978-0-12-397022-0.00003-0.
[50] Y.A. Dudnik, Metallographic inspection of The Metal-Enamel contact Zone, Met. Sci. Heat Treat. 25 (1983) 472–475, https://doi.org/10.1007/Bf00802317/Metrics.
[51] N.I. Min'ko, T.A. Matveeva, Glass enamels for steel and cast-iron articles, Glass Ceram. 56 (1999) 358–363, https://doi.org/10.1007/Bf02681342/Metrics.
[52] B.W. King, H.P. Tripp, W.H. Duckworth, Nature of adherence of porcelain enamels to metals, J. Am. Ceram. Soc. 42 (1959) 504–525, https://doi.org/10.1111/J.1151-2916.1959.Tb13567.X.
[53] Y.A. Dudnik, Distribution of the chemical elements of cast iron in the iron-namel contact Zone, Chem. Pet. Eng. 15 (1979) 790–795, https://doi.org/10.1007/Bf01176235/Metrics.
[54] C.A. Zapffe, Cause of defects in Enamel fired on cast iron at temperatures above 725 °C, I, J. Am. Cer. Soc. 25 (7) (1942) 175–180, https://doi.org/10.1111/J.1151-2916.1942.Tb14197.X.
[55] D. Yan, et al., Study of lower temperature–sintered enamel coating on steel bars: effect of coating cycles, J. Mat. Civ. Eng. 32 (2020) 04020262, https://doi.org/10.1061/(Asce)Mt.1943-5533.0003346.
[56] A.A. Zaitsev, V.S. Mogil'chenko, Enamel coatability of decarburized iron, Chem. Pet. Eng. 3 (4) (1967) 307–309, https://doi.org/10.1007/Bf01136435/Metrics.
[57] A.A. Zaitsev, V.S. Mogil'chenko, Improving the enamelling properties And quality of cast iron equipment", Glass Ceram 25 (1968) 93–96, https://doi.org/10.1007/BF00675989.
[58] W. Vogel, Glass Chemistry, second ed., Springer, Berlin Heidelberg, 1994 https://doi.org/10.1007/978-3-642-78723-2.
[59] F. Russo, S. Rossi, A.M. Compagnoni, Porcelain enamel coatings, Encyclopedia 1 (2021) 388–400, https://doi.org/10.3390/Encyclopedia1020032.
[60] M.S. Shekhawat, A review paper on glass-ceramics, Int. J. Mater. Phys. 6 (1) (2015) 1–6.